Modeling Glaciation of the Hellas Basin, Mars, for a 'Cold and Icy' Late Noachian Paleoclimatic Scenario

J. L. Fastook[1] and J. W. Head[2]

[1] Climate Change Institute, University of Maine, Orono, ME 04469 USA.

[2] Department of Earth, Environmental and Planetary Science, Brown University, Providence, RI 02912 USA.

Corresponding author: James Fastook (fastook@maine.edu)

Highlights:

- We use climate and ice sheet models to assess predicted Late Noachian glaciation at Hellas.
- The models predict that ice accumulates on eastern Hellas rim, flows downslope on basin wall; slope promotes shear heating, melting.
- Predicted glacial system extends across basin floor, stabilizes, ablates; sequestered by debris cover.

Key Words: Mars Climate, Mars Atmosphere, Mars Surface

Abstract

Global climate models (GCM) predict snow accumulation/glaciation on the Hellas basin eastern rim, where Amazonian glacial landforms are observed. We explore GCM results for Late Noachian-Early Hesperian higher atmospheric pressure/higher obliquity/faint young sun conditions, assess accumulation rates, and use these as input to an ice sheet model. We assess ice sheet growth, thickness, basal temperatures, basal melting water volumes, flow/sliding-ice velocities and the fate of basin floor glacial ice/meltwater. We conclude that significant volumes of glacial ice (with shear-induced basal melting) could have flowed down the basin wall and onto the basin floor, covering the majority with glacial ice. Late Noachian water budgets of up to 1000 m global equivalent layer (GEL) and Hellas floor ice sequestration are implied. Subsequent emplacement of Hesperian volcanic plains superposed on the ice may have caused melting (contact/deferred) and deformation (loading-induced flow/diapirism), potentially accounting for several observed basin floor geologic units.

1 Introduction

The Hellas impact basin, the most prominent feature in the southern hemisphere of Mars (Figure 1a) plays an extremely important role in the geologic evolution of Mars. Its formation marks the beginning of the Noachian Era (Tanaka et al. 2014; Fassett and Head, 2011), and its large diameter, extreme depth and significant asymmetry have made it a focus of attention for key problems in understanding atmospheric circulation and climate, and their evolution (e.g., Haberle et al., 2001; Forget et al, 2006; Kahre et al., 2020; Holt et al., 2008; Scanlon et al., 2018; Bernhardt et al., 2016a, 2019; Weiss and Head, 2017).

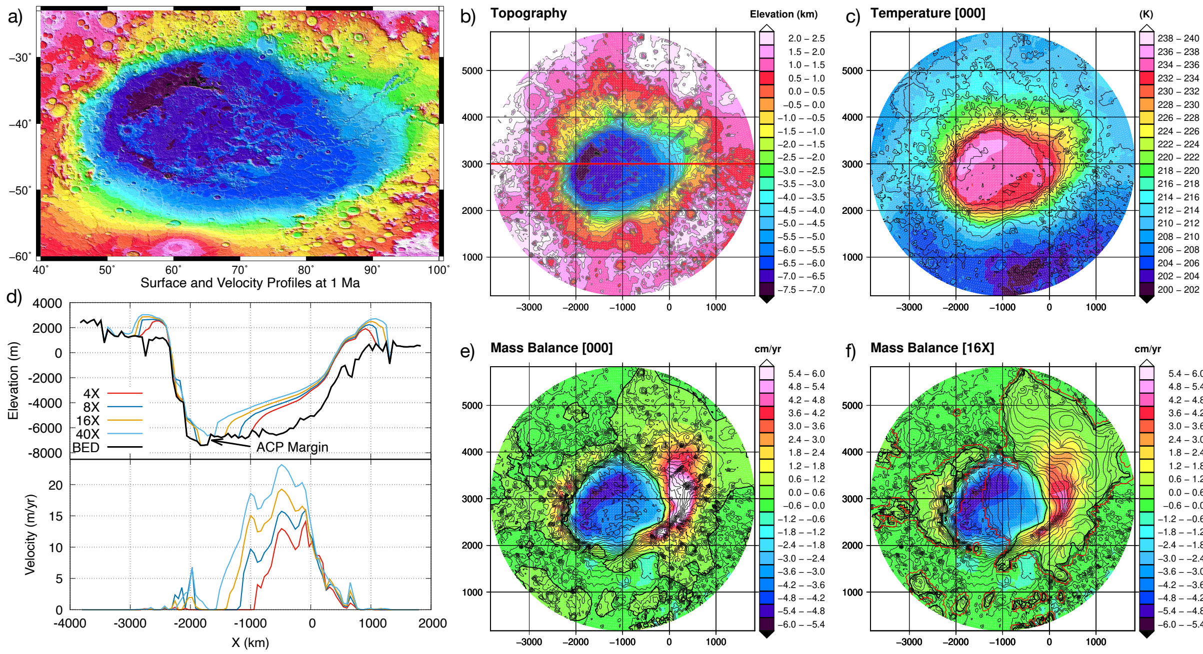

Figure 1: : a) Topographic map of Hellas basin (Smith et al. 2001), b) Grid of topography input to the model, c) Surface temperatures from the GCM input to the model, d) Profiles of surface and bed (vertical exaggeration 500X) and velocities from West to East along the red line shown in b) for four supply limits modelled, e) Initial mass balance from the GCM, f) Mass balance as the supply limit is reached and the accumulation component is reduced.

The floor of Hellas (Figure 1b) is the site of the highest atmospheric pressure and warmest temperatures on Mars (Wordsworth et al. 2013, Scanlon et al. 2018, Forget et al. 2013; Palumbo and Head, 2019) and its presence significantly influences global atmospheric circulation, eolian processes and dust accumulation. It hosts unusual deposits interpreted to represent the former presence of glaciation (Kargel & Strom 1992) and both Noachian and Hesperian lakes/oceans (Moore & Wilhelms 2001). The Hellas rim and inner slopes are significantly asymmetric (Wichman & Schultz 1989) (Fig. 1) and were modified by Early Hesperian volcanic centers (Hesperian Planum and Malea Planum) (Crown et al., 1992; Ivanov et al., 2005; Williams et al. 2009) leading to Hesperian ridged volcanic plains on the walls and floor (Tanaka & Leonard 1995; Leonard and Tanaka, 2001). Valley network systems, and several major Late Hesperian outflow channels debouch onto the basin floor (Tanaka & Leonard 1995). Ruell Vallis, a large and extensive fluvial channel on the eastern wall of Hellas Basin (Mest and Crown, 2001) has been interpreted to have formed subglacially (Cassanelli and Head, 2018), implying the presence of a melted bed (Ji et al. 2023). This range of geological activity and sequence of events has resulted in an extremely complex stratigraphy of the basin rim (Brough et al., 2016), wall (Voelker et al., 2018), floor and its surroundings (Crown et al., 2005; Bernhardt et al. 2016a, 2016b, 2019).

One of the key factors linking events in this complex history is the hydrological system/cycle, its nature and state (vertically integrated or horizontally stratified; Head, 2012), the implications for the dominant (ambient) climate conditions and the role of related aqueous processes. Two end-member models for Noachian Mars atmospheric and climatic conditions are 'warm and wet' and 'cold and icy'.

The 'warm and wet' climate is predicted to have a mean annual temperature (MAT) greater than 273 K, atmospheric pressure greater than 1 bar, and global surface-near-surface water budget 1-5 km global equivalent layer (GEL) (Craddock and Howard, 2002; Ramirez et al., 2014; Luo et al., 2017; Ramirez and Craddock, 2018; Ramirez et al., 2020; Steakley et al., 2023).

The 'cold and icy' climate is predicted to have a mean annual temperature ~226 K, atmospheric pressure in excess of several hundred millibars (Wordsworth et al. 2013, Forget et al. 2013; Palumbo et al. 2018), and global surface-near-surface water budget unknown, but thought to be in excess of several hundred meters GEL (e.g., Scanlon et al., 2018, ~136 m; Rosenberg et al., 2019, >640 m).

Intermediate between these two end members is the possibility of the 'cool and wet' climate (Kamada et al., 2022). Such a climate is characterized by seasonal excursions of the temperature above and below the melting point. Using an ice sheet model analogous to ours, Kamada et al. (2022) performed similar simulations with coupled climate and ice sheet models (PMGCM and ALICE) for a thicker 2 bar CO_2 atmosphere with up to 3% added H_2 and a 500 m GEL supply limit. The high pressure and additional H_2 was necessary as the goal was to generate a climate with regions with mean annual temperature above the freezing point, as they were interested in quantifying runoff from surface and basal melting that carved the Valley Networks. The bulk of their simulations were generated on terrain with Tharsis removed, although they did provide one simulation done on current topography that compares well with our simulation that focuses primarily on the Hellas Basin.

To further assess the fit of the model to the predictions (Cleland, 2001, 2002) of the 'cold and icy' atmosphere model, we explore the results of atmospheric GCMs that predict snow and ice accumulation and glacial flow in the south polar and southern high altitude/latitude regions (Wordsworth et al. 2013, Scanlon et al. 2018, Forget et al. 2013). The GCM results used (Scanlon et al. 2018) are for a 1 bar CO_2, 42 degree obliquity climate under a faint youg sun. The higher pressure results in warmer temperatures, 224 K for the global mean average, compared with the present 215 K global mean (Millour et al. 2018). For comparison Figure 2 shows both the present distribution of mean annual temperature from the Mars Climate Database (Millour et al. 2018) and from the GCM model (Scanlon et al. 2018). Notable is the fact that the present climate is latitude-dependent, whereas the higher-pressure model is much more elevation-dependent with a pronounced adiabatic lapse rate.

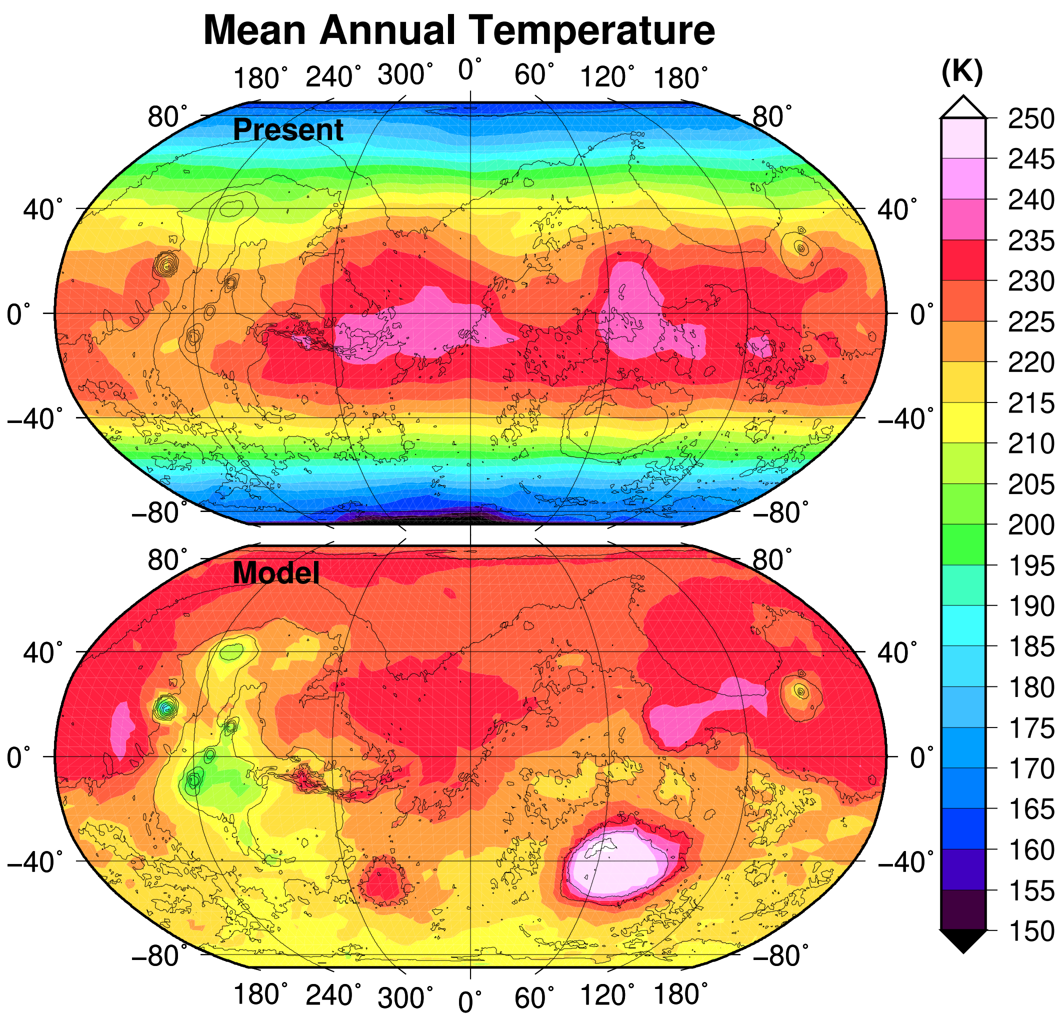

Figure 2: Mean annual temperatures for the current climate (top) from the Mars Climate Database (ref) compared with the results of the GCM (bottom) contrasting the latitude-dependence of the current climate with the elevation-dependence in the 1 bar CO2 atmosphere of the GCM.

We call on the University of Maine Ice Sheet Model (UMISM, Fastook and Prentice, 1994), a Glacial Flow Model (GFM) to assess the role of ice accumulation, the nature of glacial ice flow, the possible presence and significance of basal melting and erosion, and the fate of meltwater in the ablation zone on the Hellas basin floor. We use these predictions, together with snow and ice accumulation rates, to model and assess the accumulated ice thickness, glacier thermal structure, flow rates, basal thermal regime (cold-based or wet-based), and the possible presence of slope-related shear heating/melting during the Late Noachian/Early Hesperian according to the ‘cold and icy’ model.

We focus on the eastern Hellas basin rim due to the wide range in topographic elevations (Figure 1b), the extended geological record of Mars history (base of Noachian to Amazonian), the wide diversity of geomorphic features observed there (e.g., Tanaka and Leonard, 1995; Carr and Head, 2010), and the fact that snow and ice accumulation and glaciation have been independently predicted (Wordsworth et al. 2013, Scanlon et al. 2018, Forget et al. 2013) and documented (e.g., Holt et al., 2008; Head et al., 2005). In this study, we use the results of these independent analyses and apply glacial flow modeling to assess the implications for the evolution of the Hellas basin eastern rim, wall and basin floor.

Figure 3, which contrasts various of the inputs and outputs of the GFM, shows a transect through the modelled domain along the centerline shown by the red line in Figure 1b for the 16X case also documented in Figures 1d,f. Along the bottom is a repeat of Figure 1b for the 16X case, this time with thickness indicated by the red line. Above this is the mass balance (as in Figure 1f). This shows the two accumulation areas on either rim of Hellas, with the major ablation zone in the basin. Notable is that the eastern flow is approximately half in the accumulation zone and half in the ablation zone, with a clear equilibrium line (zero mass balance) at -250 km. Above this is the contribution of internal heat as the fraction of the provided geothermal flux (55 mW/m^2) developed from shear deformation and basal sliding that will be discussed in detail later. This amounts to a few percent in the ablation zone where the bed is melted and sliding is occurring, to up to 9 percent in the accumulation zone where the bed is frozen. Above this is the input surface temperature from the GCM (black line) as well as the basal temperature calculated by the GFM (blue line). A major area of melted bed appears on the eastern slope, mostly in the ablation zone, with a few patches where the bed is melted further up the slope and on the western rim. Finally the top panel shows basal melt rates in those areas where the bed reaches the melting point with as much as 4 cm/yr of basal melting.

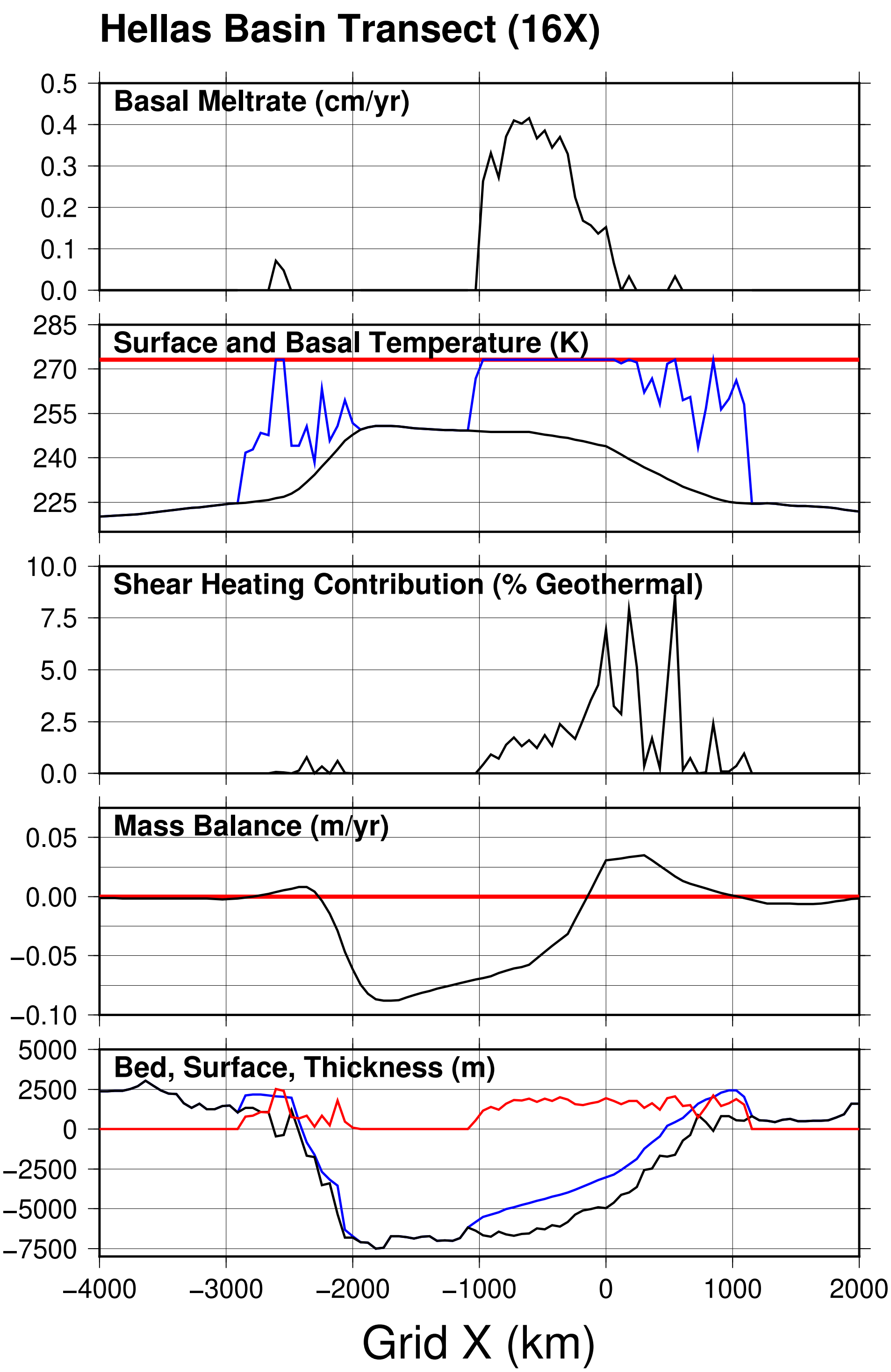

Figure 3: Transects along the red line of Figure 1b with from bottom to top, bed, surface, and thickness; mass balance showing accumulation and ablation zones; internal heat contribution as percentage of the supplied geothermal flux (55 mW/m2); the input surface temperature from the GCM and the calculated basal temperature from the GFM; and the basal melting rate in areas where the bed reaches the melting point.

2 Modelling

2.1 UMISM and the Supply Limit:

The University of Maine Ice Sheet Model (UMISM) adapted for Mars is a shallow-ice approximation, thermomechanical model described in detail in Fastook and Prentice (1994). UMISM is run in a "supply-limited" mode where only a finite amount of water is available to build ice sheets. A limit on the amount of available water with which to build ice sheets is necessary, because unlike Earth that has basically unlimited water available in the form of the oceans, the amount of water on Mars in the past is both much smaller, as well as being poorly constrained. Estimates range from twice the current estimated inventory of 34 m GEL (Carr and Head 2015) to 640 m GEL (Rosenberg et al., 2019). Even higher estimates from 400 to 1250 m GEL are associated with the presence of a northern ocean (Cardenas and Lamb, 2022). We examine the footprint of various modelled ice sheets for supply limits ranging from 1X (34 m GEL) to 40X (1360 m GEL).

This requires processing of the GCM models as follows: a run is performed that starts with uniform ice coverage and tracks the ice thickness through one or more years. This approach is utilized so that we can determine where, and at what rate, ice accumulates, and in addition to learn how rapidly it would be removed in areas with negative net mass balance. The ice thickness history at each point is tracked for periods where ice is thickening, which contributes to the accumulation rate, as well as where it is thinning, which contributes to the ablation (removal) rate. The net annual mass balance (accumulation minus ablation) is then the input required by UMISM. Using this approach and these results, we obtain information about how rapidly ice that flowed into a region where the net mass balance is negative, would be removed. This also allows us to independently reduce only the accumulation rate as the ice sheet approaches the supply limit.

Two examples are shown in Figure 4a. The blue and red curve (at 41.25 S, 39.375 E) shows a loss of thickness of 49 mm over the 669 sols of model run time, equivalent to a negative net mass balance of -27 mm/yr. By keeping track of when the ice layer is thickening (red, accumulation) and when it is thinning (blue, ablation) we separate this into a thickening of 26 mm (14 mm/yr. accumulation rate) and a thinning of 75 mm (41 mm/yr. ablation rate). Note that these combine to yield the same net mass balance, -27 mm/yr, that one obtains by simply examining the beginning and endpoints.

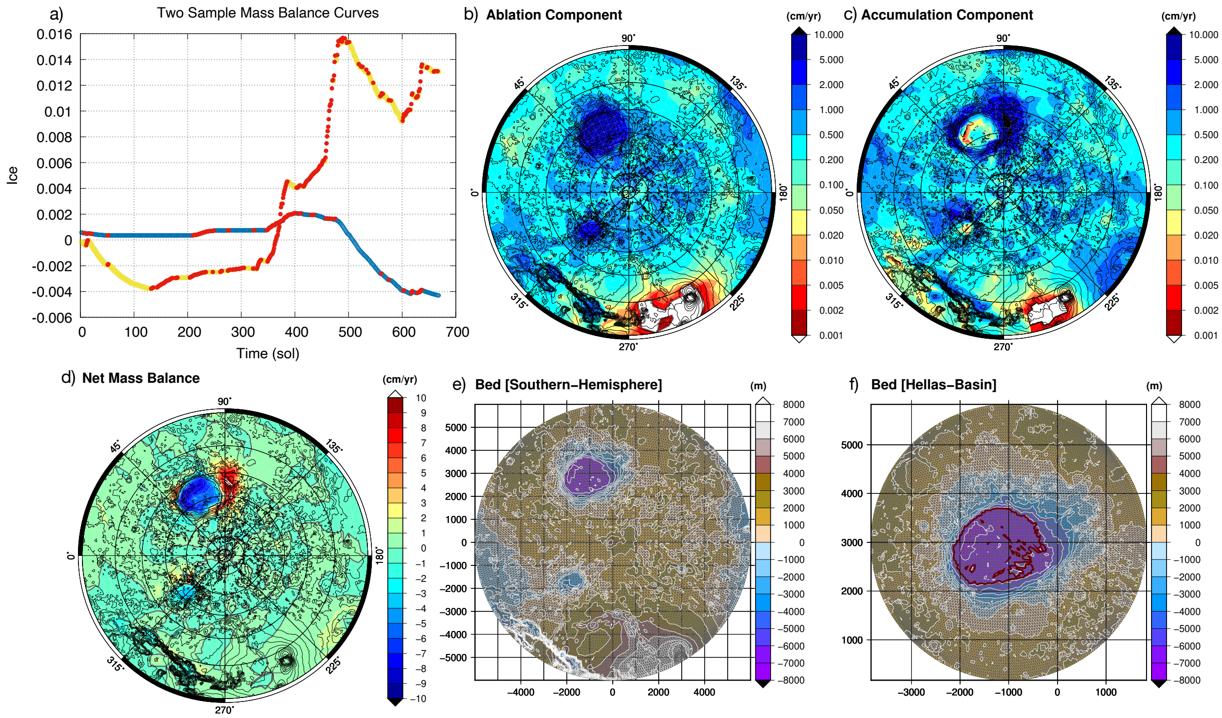

Figure 4: a) Two sample ice surface curves (blue and red at 41.25 S, 39.375 E, and yellow and red, at 41.25 S, 45.0 E). Red indicates thickening and is summed into the accumulation component, whereas yellow and blue indicate thinning that is summed into the ablation component. b) Ablation component, c) accumulation component, and d) net mass balance (the difference of the two). Bed elevation for e) the whole southern hemisphere grid (~100 km spacing) used to define the supply-limiting parameter above, and f) the higher-resolution (~50 km spacing) focused Hellas basin region domain with basin floor outlined in red. Both e) and f) each have 10,000 nodes and 9801 elements, outlines of which are shown in the Figure by gray triangles, pairs of which comprise a single quadrilateral element. The red outline in f) is the area we define as the basin floor in Table 1.

A climate model that only tracked ice deposition through a martian year starting with zero ice thickness would see the 26 mm deposited and then completely removed before the end of the year. Examining only the beginning and endpoints (zero and zero) one would conclude that the net mass balance was zero, and one would have no information ablout the potential for ablation. Knowing the potential for ablation (in this case the potential to removal 75 mm) is critical since expanding ice sheets grow out of the accumulation zone into the ablation area, which they necessarily will do as they grow towards a steady state where whole ice sheet net accumulation is exactly balanced by net ablation.

The yellow and red curve in Figure 4a shows an example (at 41.25 S, 45.0 E) that displays an overall increase in thickness of 131 mm, yielding a positive net mass balance of 72 mm/yr. A similar separation into thickening (red) and thinning (yellow) yields an accumulation component of 283 mm (154 mm/yr) and an ablation component of 152 mm (83 mm/yr). Again, a simpler climate model without the initial ice layer would yield the same positive net mass balance (72 mm/yr), but with no information about the potential for ablation.

Figures 4b,c,d show polar stereographic projections of the entire southern hemisphere for both these ablation and accumulation components, as well as the resulting net mass balance. Two of the largest areas of most extreme ablation and accumulation occur in the deepest part of the Hellas Basin and on its western rim respectively. There is another smaller region of accumulation on the eastern rim of Hellas, and the Argyre Basin shows a similar but more muted pattern.

In UMISM, with net mass balance separated into accumulation and ablation components, we can now modify the mass balance to reflect the fact that the ice sheet is approaching its supply limit. This is done by linearly reducing the accumulation components proportional to how close the volume of the ice sheet is to the supply limit (i.e. when the ice sheet volume equals the supply limit the accumulation component is uniformly zero). In practice this rarely falls below 40% since the unchanging ablation component reduces the areal extent of the ice sheet as its accumulation area is reduced. As it reaches its steady state thickness (that configuration where the net accumulation of the entire ice sheet is exactly balanced by net ablation), volume stops changing as does the reduction of the accumulation component.

Generic Mapping Tool's mapproject function is used to project the latitude/longitude coordinate system of the LMD GCM results and the MOLA topography (Smith et al. 2001) onto the cartesian X/Y coordinate grid used by UMISM. The projection is General Stereographic with the origin at the south pole and the y-axis along 90E longitude using the provided Mars Ellipsoid (a=3396190, 1/f = 169.8944). Interpolation of values from the lower resolution GCM to the higher-resolution grid used by UMISM is bi-linear quadrilateral interpolation among the nearest neighbor in each of the four quadrants using Finite Element shape functions.

UMISM has the capability to run 'embedded' models, whereby the enclosed focused region with higher resolution obtains boundary conditions from the lower-resolution encompassing region. This feature is used to generate the reduction parameter from a lower-resolution grid (~100 km, Figure 4e) that covers the entire southern hemisphere so that the reduction in accumulation is driven not by the volume generated in our higher-resolution (~50 km, Figure 4f) Hellas basin domain, but by the broader regional growth in the whole southern hemisphere. Each of these grids have 10,000 nodes for computation using UMISM's finite-element method (Becker et al. 1981). In Figure 4f, a red line shows the outline of the Hellas basin floor that is below -6200 m, used in the analysis found in Table 1. Also shown in Figures 4e,f are the outlines of the distorted checkerboard of elements used in the UMISM finite-element method.

An example of the GFM results is shown in Figure 5a for the Hellas grid for a 16X supply limit. Area increases very rapidly as the small initial volume produces little reduction of the accumulation component, which therefor is at its maximum value. The resulting ice sheet footprint obtains its largest extent in under 10,000 years. The area remains relatively constant until 100,000 years because the ice has not developed sufficient flow during that time to be growing out into the surrounding ablation area. The volume grows more slowly, but by 100,000 years growth slows as the reduction factor approaches 65%. From 100,000 to 1,000,000 years, area decreases while volume remains relatively constant as the reduction factor continues to decrease, driven by the reduction factor curve generated by the full southern hemisphere grid.

All supply limit cases (1X, 2X, 4X, 16X, and 40X, where 1X = 34 m GEL or 5 Mkm^3; Carr and Head, 2015) are run for 1 million years, at which point the parameter representing the ratio between the current volume and the supply limit has stabilized (Figure 5b). This parameter is used to reduce the accumulation component of the net mass balance, while leaving the ablation component unchanged.

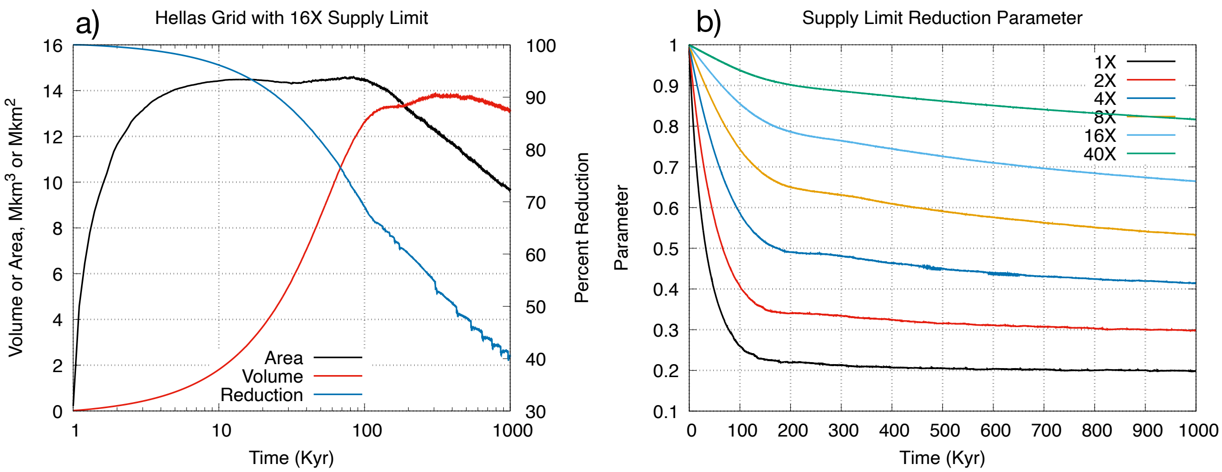

Figure 5: a) Area, volume, and reduction curve for Hellas grid with 16X supply limit. b) Supply limiting parameter.

Tabulated results for the various supply limits are shown in Table 1. These include the grid area, how much of that area is covered with ice, the ice volume, average thickness, area with a melted bed, as well as the basal meltwater production rate. These results, along with surface meltwater production, are also provided for the basin floor, the region below -6200 m elevation shown in Figure 4f by the red outline.

Table 1: Supply Limit Results at 1,000,000 years							
Supply Limit	Units	1X	2X	4X	8X	16X	40X
Supply Limit	GEL	34	68	136	272	544	1360
Supply Limit	Mkm^3	5	10	20	40	80	200
Full Model	10,000 Nodes, 9801 Elements, Grid Resolution 50 km						
Grid Area	Mkm^2	25.13	25.13	25.13	25.13	25.13	25.13
Ice Area	Mkm^2	4.26	5.97	7.90	10.31	12.76	15.01
Percent ice Cover	%	16.95	23.73	31.43	41.03	50.75	59.73
Average Thickness	m	1078	1331	1292	1306	1337	1417
Ice Volume	Mkm^3	4.60	7.94	10.21	13.47	17.05	21.27
Ice Volume	GEL	31.73	54.82	70.50	93.02	117.8	146.9
Ice Area with Melting	Mkm^2	0.681	0.973	1.891	2.471	3.061	3.874
Percentage of Area Melted	%	15.98	16.31	23.94	23.96	23.99	25.81
Basal Water Melt Rate	km^3/yr	17.31	42.43	322.8	785.8	1475	2815
Basal Water Melt Rate	GEL/Kyr	0.120	0.293	2.229	5.427	10.18	19.44
Basin Floor Only	All Nodes with Elevations Less Than -6200 m						
Basin Floor Area	Mkm^2	2.324	2.324	2.324	2.324	2.324	2.324
With Ice Area	Mkm^2	0.093	0.312	0.712	1.110	1.535	2.044
Percent ice Cover	%	4.01	13.42	30.61	47.77	66.05	87.93
Average Thickness	m	863	1244	1350	1480	1611	1761
Maximum Thickness	m	1909	2479	2591	2848	3095	3333
Ice Volume	Mkm^3	0.080	0.388	0.951	1.643	2.473	3.598
Ice Volume	GEL	0.556	2.678	6.634	11.35	17.08	24.85
Ice Area with Melting	Mkm^2	0.045	0.181	0.562	0.841	1.237	1.738
Percentage of Area Melted	%	1.932	7.764	24.17	36.17	53.24	74.76
Basal Water Melt Rate	km^3/yr	1.339	7.333	113.7	307.4	701.9	1473
Basal Water Melt Rate	GEL/Kyr	0.009	0.051	0.784	2.123	4.847	10.17
Area with Ablation	Mkm^2	0.093	0.181	0.712	1.110	1.535	2.044
Percentage of Area Ablated	%	100.0	100.0	100.0	100.0	100.0	100.0
Surface Ablation Rate	km^3/yr	20.51	65.52	138.0	202.6	261.3	324.9
Surface Ablation Rate	GEL/Kyr	0.142	0.453	0.953	1.399	1.805	2.244

Table 1: Summarizing the results from the various Supply Limits imposed on the ice sheet model for both the entire Figure 4f. domain as well as for the basin floor below -6200 m elevation (the red outline).

The area of the ice sheet for various supply limits is shown in Figure 6a. Each begins at about 14 Mkm^2, the areal footprint of which is shown by the area with positive mass balance in Figure 1d. As the volume increases, reducing the supply-limit parameter that reduces the accumulation component, the regions with positive net mass balance shrink and the ice sheet contracts into the area where the accumulation component is largest. Supply limit cases 1X to 8X decrease monotonically, whereas 16X and 40X initially decrease before later growing larger as ice flows from regions of positive net balance into ablation areas.

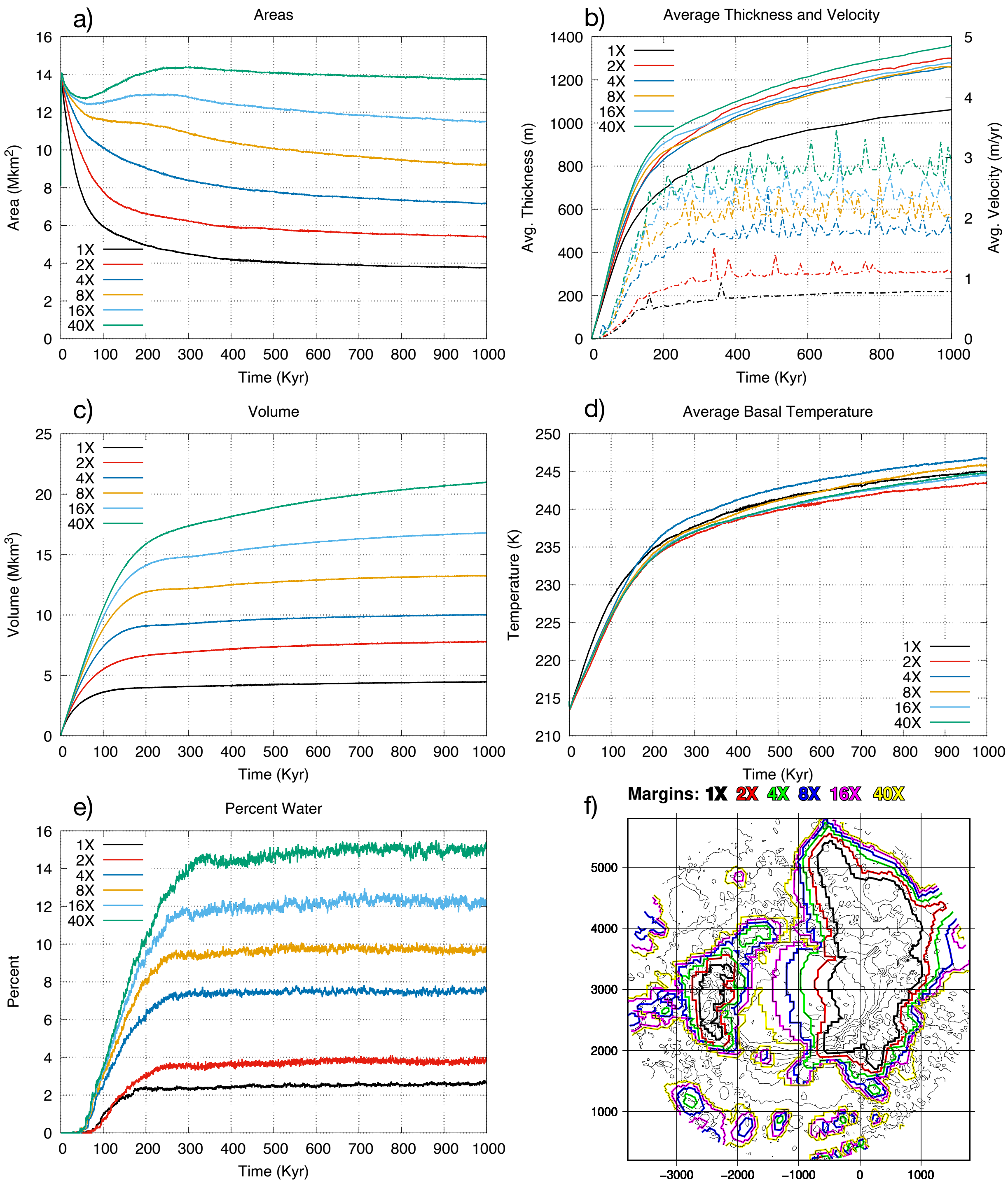

Figure 6: a) Area of the ice sheets, b) Average thickness (solid lines) and average ice velocity (dashed lines) c) Ice sheet volumes, d) Average basal temperatures, and e) Percent of the ice sheet area that reaches the melting point and begins to produce basal meltwater for various limits over the 1 million years of model simulation. f) Margin outlines for various supply limits ranging from 1X (Black) to 40X (Yellow).

The average thicknesses and average velocities for the various supply limits are shown in Figure 6b. With the exception of the 1X case, supply limit has little effect on thickness. Velocity clearly trends with available supply, with larger limits permitting faster flow. It is worth noting that significant flow does not begin to occur until average thickness has reached ~800 m, after which it remains constant.

Ice sheet volumes for various supply limits are shown in Figure 6c. Cases 1X to 16X have clearly reached an equilibrium state where growth has depleted the supply (Figure 5b). With further growth the accumulation component would be further reduced, resulting in overall shrinkage of the ice sheet back to its equilibrium configuration. Only the 40X case is still growing after 1 million years.

The average basal temperatures for the various supply limits are shown in Figure 6d. All start at 215 K, the average surface temperature defined by the GCM (Figure 1c). As ice thickens, insulating the bed, average basal temperatures increase, with little difference among the different supply limit cases.

The percentage of the ice sheet area that reaches the melting point is shown in Figure 6e. Note that no melted bed appears in any case until ~50,000 years, at which time the average thickness in all cases is ~400 m. All increase rapidly after this point, reaching a plateau at between 180,000 (1X) and 300,000 (40X) years. Much of the increase in melting area for the larger supply limits is due to the ice sheet growing further into the warmer ablation zone on the floor of the Hellas basin (Figure 1e).

The contours of zero ice thickness representing the margin outlines of the ice sheet for various supply-limit cases are shown in Figure 6f. The 1X case (black) is largely confined to the basin rim with only minor flow down the eastern wall. For the largest supply-limit case, 40X (yellow), flow reaches far into the basin and even merges with ice from the western wall.

2.2 UMISM Thermodynamics:

The thermodynamics of the ice is dictated by the boundary conditions, in particular the specified surface mean annual temperature and the basal geothermal heat flux, with additional internal heat sources generated from shear heating. The interaction between the thermodynamic properties (internal and basal temperatures, melted bed) and the mechanical properties of the ice (ice hardness, presence of lubricating water at the bed that leads to sliding) is complex. Thicker ice tends to be warmer throughout the column and at the bed due to the insulating properties of the overlying ice defined by the geothermal flux. This source of heat entering the base of the ice column can also be expressed as a temperature gradient in the form of the conductivity. The geothermal flux considered here, 55 mW/m^2 (Grott and Brauer, 2010), corresponds to a temperature gradient in the ice between 24 K/km (for ice at the melting point) to 18 K/km (for ice at 226 K). For example, an ice column with a surface temperature of 226 K would need to be approximately 2.25 km thick for the bed to reach the melting point (an average temperature within the column of 250 K corresponding to a temperature gradient of 21 K/km).

The additional source of heat, shear heating, that adds to that of the geothermal flux, occurs in two ways: 1) as heat generated in the ice column, expressed a twice the product of strain rate (the gradient of the horizonal velocity, the column-average of which is shown in Figure 7d), and stress (a linear variation of the driving stress from zero at the surface to its maximum value at the bed that is shown in Figure 7a), and 2) friction at the bed that accompanies sliding, in this case expressed as the product of the sliding velocity and the basal shear stress.

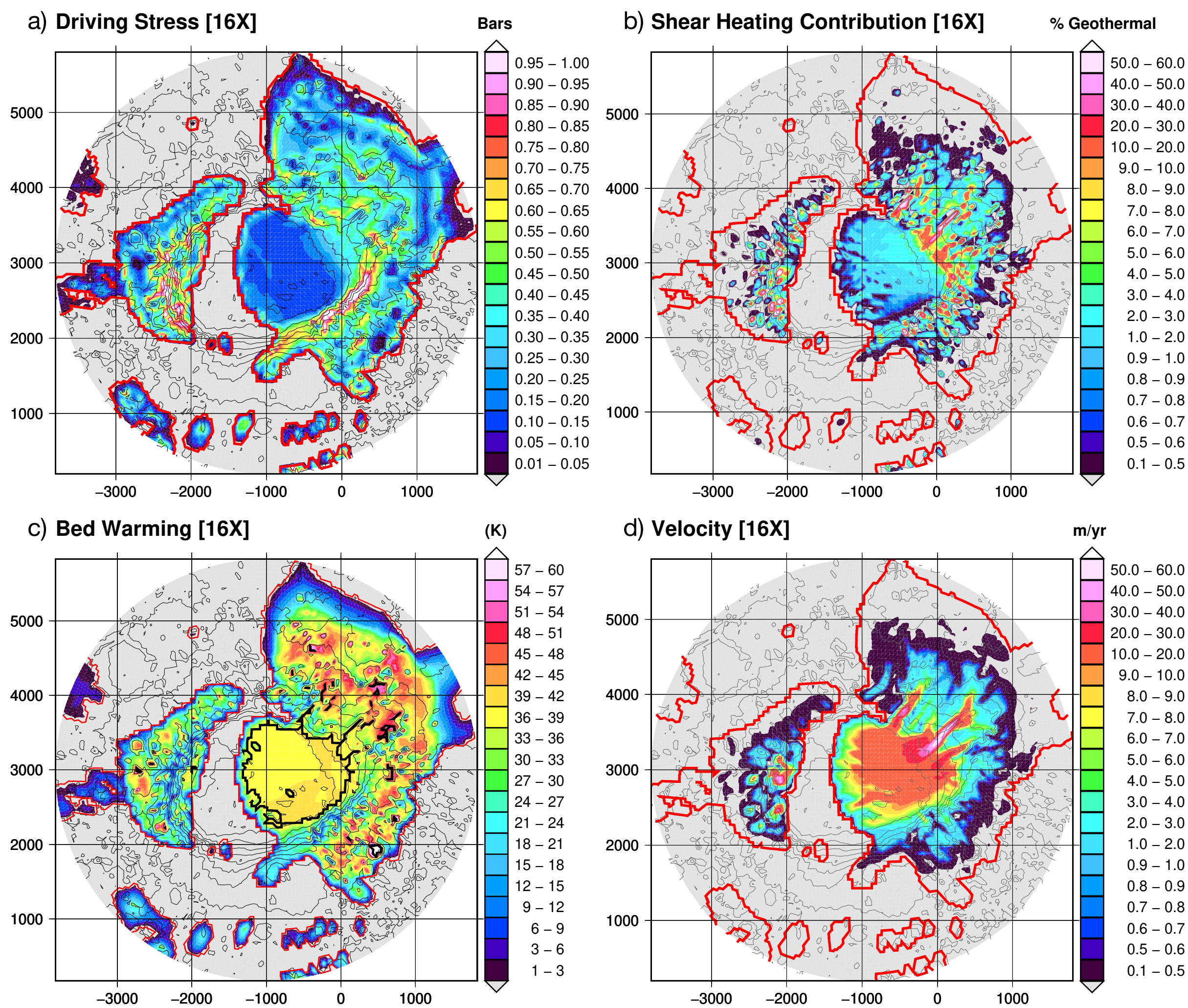

Figure 7: a) Driving stress, b) shear heating contribution as percentage of geothermal flux (55 mW/m²), c) bed warming, the difference between GCM-specified surface mean annual temperature and basal temperature, with region at the melting point outlined in black d) resulting ice velocity.

Sliding occurs where the bed is lubricated by meltwater produced when the bed reaches the melting point, shown by a heavy black outline in Figure 7c. Figure 7c shows the amount of warming of the bed relative to the specified surface temperature that depends primarily on the ice thickness and geothermal flux (augmented by any additional shear heating). A warmer bed also implies warmer conditions throughout the ice column; this affects the mechanical properties of the ice, making it softer and less resistant to deformation.

The result is lower slope, and consequently lower driving stress (proportional to the product of ice thickness and surface slope), as the ice is both warmer and there is less resistance. This is apparent in the dark blue region on the floor of the basin in Figure 7a. However, the faster flow (the red in Figure 7d) results in significant shear heating, shown as the percentage of the 55 mW/m^2 geothermal flux in Figure 7b.

On the eastern Hellas basin wall the situation is more complex, with narrow "streams" of melt-produced sliding (see Figure 12) separated by frozen bed regions where internal deformation flow is occurring. In the sliding streams the driving stress may be less, but the velocity is higher. In the flow regions, velocity may be lower, but the driving stress is larger, producing shear heating that contributes up to an additional 50% of the value of the geothermal flux. This warms the ice column more than would be produced by the geothermal heat flux alone.

2.3 Debris Cover from Sublimating dusty ice (MSIM):

MSIM, a suite of programs that can calculate the buildup of lag as an ice layer with a specified dust content sublimates (Schorghofer 2010) was adapted to assess orbital predictions from a solution for Mars over the last 21 million years (Laskar et al. 2004), shown in Figure 8a. MSIM, as we have used it, only considers the removal if ice by sublimation and vapor transport through the overlying debris layer, which as it thickens slows the rate of sublimation. The initial rate is quite high, dropping by an order of magnitude as the lag layer forms from the dust content of the ice. A layer of fresh snow deposited on top of the lag would sublimate rapidly, contributing its dust load to the lag layer, but the ice beneath the lag would still be protected by the debris cover (e.g., Wilson and Head, 2009).

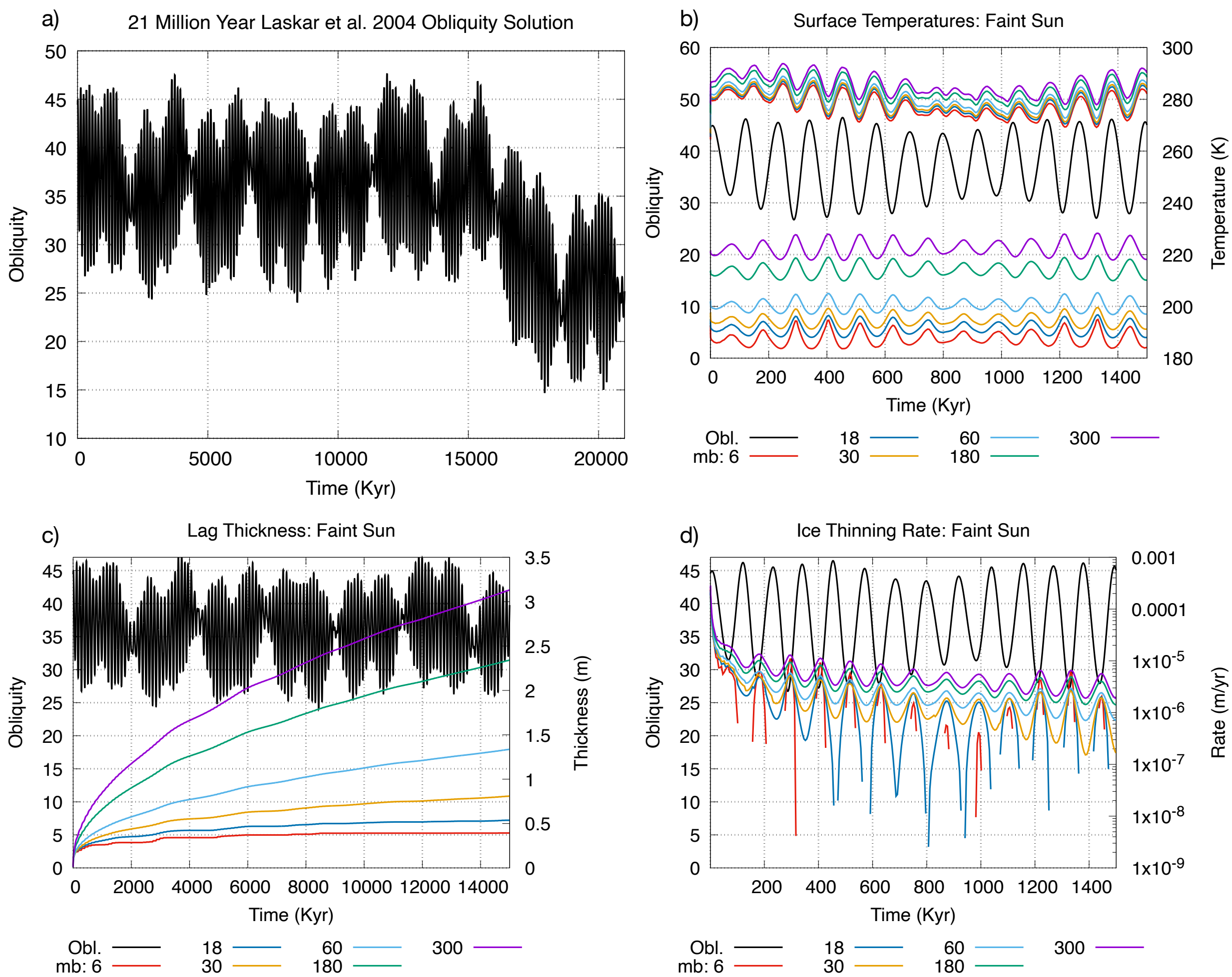

Figure 8: a) Laskar et al. 2004 solution for the obliquity of the last 21 million years. The 15 million year period where the obliquity is consistently high is used to drive the MSIM model of ice removal and lag generation. b) Surface Temperatures driven by the Laskar obliquity (black line) and well as mean annual temperatures (bottom colored lines) and peak temperatures (top colored lines). c) Lag thickness over the 15 million year modeled time. d) Ice thinning rate due to sublimation.

Laskar et al. (2004) established that the orbital solution was chaotic, such that only the most recent 20 million years was deterministic (Figure 8a). Within that period there is a pronounced shift in obliquity around 5 million years from the current relatively low average (15-35, mean 26) to a higher obliquity pattern (24-48, mean 36). Beyond that time many different solutions were presented, each with its own unique temporal pattern. Laskar et al. (2004) also established that the most probable obliquity was 42 degrees, the value used in the GCM climate simulation. MSIM, used to describe the sublimation and lag formation, accepts orbital parameters in its calculations, so we chose to use the early part of the robust Laskar et al. (2004) solution as typical of what a higher obliquity orbital solution would look like (Figure 8d).

The model is run for a latitude of 40S at an elevation of -6600 m typical of a point within the Hellas Basin. The ice is assumed to have 3% dust content, and the resulting lag to have formed as the ice sublimates, and is assumed to have a porosity of 40% (Schorghofer, 2007). Simulations were performed for 6, 18, 30, 60, 180, and 300 mbars. Surface temperatures (both mean annual and peak) for the first 1.5 million years are shown in Figure 8b for a faint young sun case (80% of current luminosity). Peak temperatures (the top set of lines, all of which are well above the melting point) are warmest during high obliquity, whereas mean annual temperatures are warmest during low obliquity. Increasing atmospheric pressure from 6 to 300 mbars raises the mean annual temperature by close to 30 K. The buildup of a lag layer for the various pressures for the full 15 million years is shown in Figure 8c, with the 6 mbar case achieving a lag thickness of 39 cm while sublimating just under 8 m ice, whereas the 300 mbar case lag thickness exceeds 3 m while removing over 60 m of ice.

Sublimation is initially rapid, the order of cm/year, but decreases by 2 orders of magnitude within a thousand years as the growing lag layer serves to insulate the ice as well as provide a barrier for the diffusion of vapor to the atmosphere. After 1 million years sublimation rates have dropped to a few microns per year, but they never decrease completely to zero, except for the lowest pressure. The rate of ice thinning by sublimation for the first 1.5 million years is shown in Figure 8d. Lag thickening is basically identical, since whatever is removed from the ice adds a specific amount to the lag layer (5.15 cm of lag for every meter of ice removed defined by the 3% dust content of the ice and the 40% porosity of the resulting lag).

Assuming that the rate of thinning shown in Figure 8d has stabilized from the transient values typical of its initial rapid thinning, we can estimate how long it would take to remove 1000 m of ice, resulting in a 50 m thick lag layer. Averaging the rates over the last million years of the 15 million years modeled, we find that for the lowest pressure (6 mbar), it would take over 90 billion years to completely remove 1000 m of ice. The higher pressure cases have higher final rates and hence remove the ice more rapidly. The 180 mbar case persists for just over 1 billion, while for the highest pressure model, 300 mbar, the 1000 m of ice lasts just 860 million years. Since the ambient atmospheric pressure history of Mars is largely unconstrained, we predict, on the basis of these results, that ice in the Hellas basin could easily persist into the present if it were ever deposited in the past. Analogous results are shown in Figure 9 for the lowering ice surface with the resulting lag layer, driven by the Laskar et al. (2004) orbital solution thought to have been typical in the past.

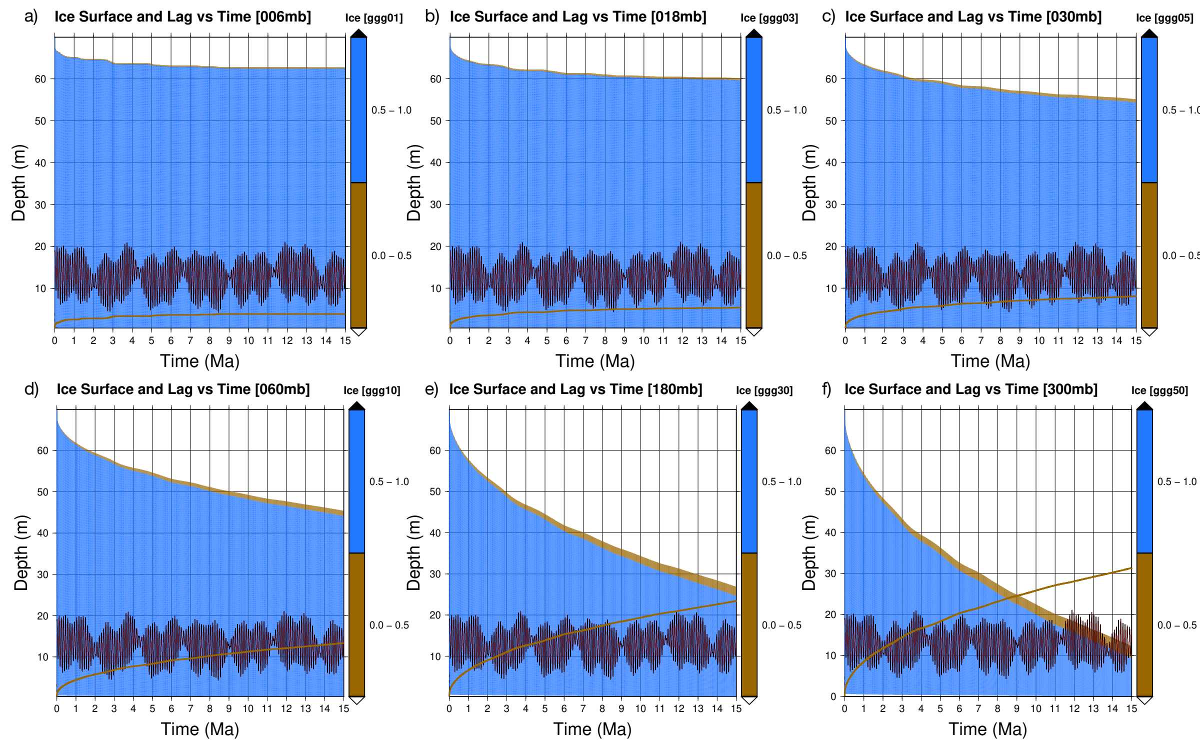

Figure 9: Ice surface and lag layer generated from 3% ice dust content and 40% lag porosity for the various pressures modeled.

3 Analysis

On the basis of the large scale and integrated nature of the ice accumulation zones, regions of flow, and zones of ablation in the Hellas region (Figure 1), we use standard terrestrial glacial terminology and refer to this region as the Hellas Glacial System (HGS). The HGS consists of inputs (precipitation), stores (mass of ice added to by accumulation and lost by ablation), transfers (glacial movements due to topographic gradient and increasing source accumulation) and outputs (ablation, consisting of melting and sublimation) (Benn and Evans, 2014).

We begin with the GCM scenario for a glaciated early Mars (Wordsworth et al. 2013, Forget et al. 2013) shown in Figures 1c,e. Scanlon (2016) and Scanlon et al. (2018) explored more than 30 climate scenarios with obliquities ranging from 15-42 degrees, pressures from 125-1000 mb, and atmospheres of pure CO_2, as well as those warmed by added grey gases. We used each scenario to provide input to a GFM (the University of Maine Ice Sheet Model, UMISM, adapted for Mars (e.g., Fastook & Head 2014, 2015; Fastook et al. 2008, 2011, 2012, 2014).

We examined in more detail the most probable obliquity scenario, ~ 42 degrees according to Laskar et al. (2004), with a 1000 mb pure CO_2 atmosphere and a faint young sun (Wordsworth et al. 2013, Forget et al. 2013). These results predicted the development of an ice sheet on the eastern Hellas rim, that flowed down the eastern wall of Hellas, almost completely covering the Hellas basin floor (Figures 1a,b). This broad region of the floor closely corresponds to the area of the Alpheus Colles Plateau (ACP). The ACP is a large (~750,000 km^2) broadly lobate, convex-to-the-west region located on the central and western Hellas basin floor, described as a thick multilayered deposit dominated by knobby and hummocky terrain (Moore and Wilhelms, 2001). It has subsequently been shown to be subdivided into a NW belt of chaotic terrain (multiple, relatively large elongated layered knobs/hills) and a relatively smoother central part containing multiple smooth lobate shapes overlying the ACP floor; these have been interpreted to have formed through a remobilization of an ice-rich deposit of possible glacial origin that was originally deposited during periods of high obliquity (e.g., Bernhardt et al., 2016a; Diot et al., 2016). The Alphaeus Colles Plateau is separated from the western Hellas floor by an arc-like scarp (Figure 1a,b; marked ACP in Figure 1d), west of which lies a region of highly deformed lower-lying deposits known as the banded terrain (Diot et al, 2016; Weiss and Head, 2017; Bernhardt et al., 2019).

The surface temperatures in this scenario showed no mean annual temperature above freezing, even on the Hellas basin floor (Figure 1c). However, the UMISM model results showed large areas of melted bed that appeared to derive from the added shear heating on the relatively steeper basin wall (Figures 7b,c). To investigate this further, an embedded region centered on Hellas with higher resolution (Figure 4f) was run using the same GCM scenario to investigate in more detail the behavior of ice flowing down the relatively steep slopes (average slope of 0.3 degrees on the eastern wall) from the large accumulation zone on the eastern Hellas rim, where accumulation rates from the GCM are predicted to be several cm/yr (Figures 1e and 4d).

How much water is available during the Late Noachian? The quantity of interest is the amount of water that is available in the surface and near-surface environment (Carr and Head, 2014, 2015). Analysis of Amazonian-aged pedestal craters (Kadish et al., 2010) and mid-latitude Amazonian glacial deposits (Fastook and Head, 2013) suggest that ice accumulation was "supply-limited": this means that the amount of ice available for mobilization and deposition was limited by the supply of water available as ice in a) the polar layered terrains or other high latitude glacial ice accumulations, b) near-surface shallow ice deposits and c) the upper regolith. Carr and Head (2015) estimated the current near-surface water budget as an ~34 m GEL (we describe this as 1X) and predicted that the Late Noachian near-surface value was about twice this value (2X). Due to uncertainties in this number (e.g., Scanlon et al., 2018, ~136 m GEL, 4X; Rosenberg et al., 2019, >640 m GEL, >18.8X) we employ a range of Late Noachian surface/near-surface water budgets as "supply-limits" in multiples of the estimated current value. Utilization of the current Mars 1X inventory produces only a limited ice sheet forming on the eastern rim and wall (Figure 10a), and does not produce any flow down onto the Hellas basin floor, consistent with observed Amazonian-aged glacial features (Head et al., 2005; Holt et al, 2008). Since we are assessing the plausibility of ice flow into Hellas, we start with a supply limit of 4X (136 m GEL), corresponding to the limit found by Scanlon et al. (2018) that agreed well with the south circumpolar Dorsa Argentea Formation (DAF) footprint. Other supply limits modelled include 8X (272 m GEL), 16X (544 m GEL), and 40X (1360 m GEL), all significantly below the 5000 m GEL proposed by Luo et al. (2017).

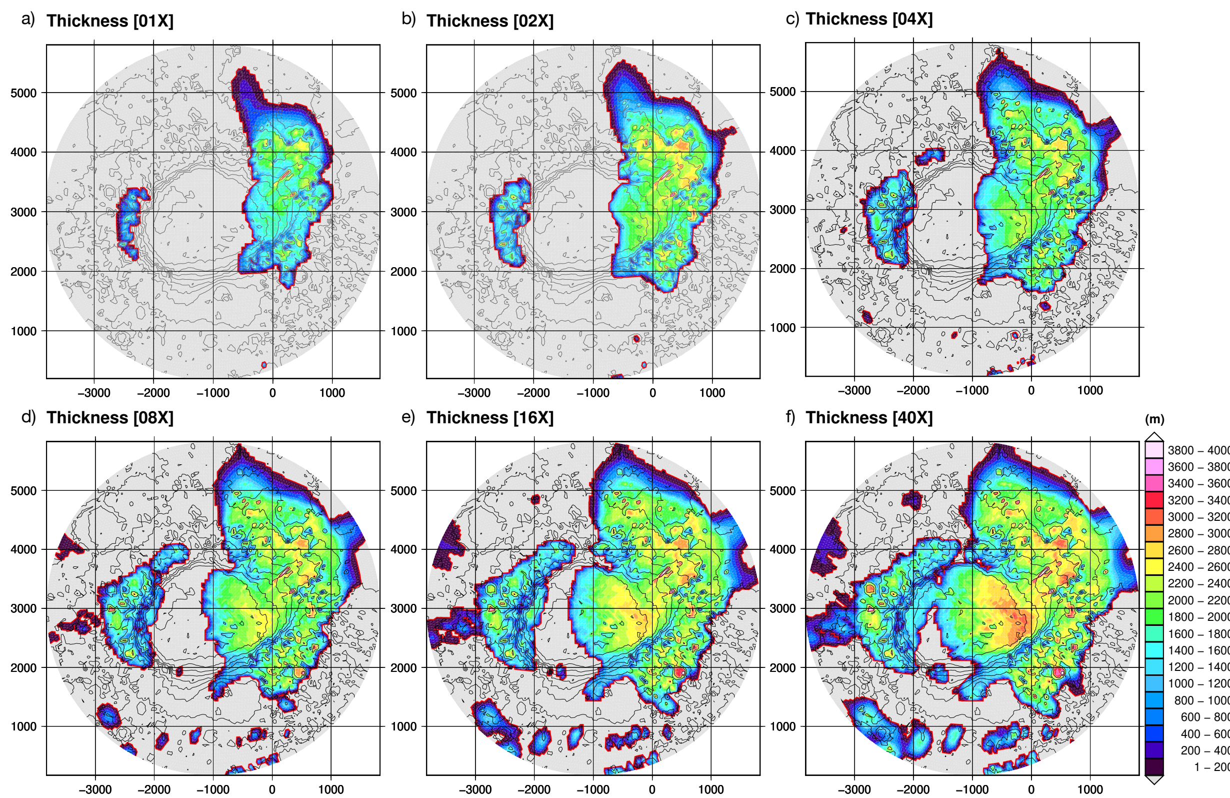

Figure 10: Ice thickness for the various supply limits.

When UMISM is run in a supply-limited mode, only a finite amount of water is available to build ice sheets (appearing as the supply-limit reduction parameter shown in Figure 5b). This process results in a reduction of the area with positive net mass balance as the accumulation component is reduced by the supply-limit reduction parameter (Figure 1f shows the resulting reduction for a 16X supply limit). Runs of 1 Ma are generally sufficient for the resulting ice sheet to reach an equilibrium configuration. Figure 1d shows profiles crossing Hellas from West to East along the red line in Figure 1b. The 4 lines show profiles for 4X (red, thinnest profile), 8X (blue), 16X (purple), and 40X (gold, thickest profile; ~1360 m GEL). The labelled scarp at -1750 km corresponds to the profile crossing the western edge of the Alpheus Colles Plateau (ACP). Glacial ice thicknesses on the Hellas floor are up to the ~2 km range. Also shown in Figure 1d are representative velocities along the profiles.

Of interest in determining the distribution and magnitude of basal melting is the bed condition. Mean annual surface temperatures from the 1 bar, 42 degree obliquity GCM results for the bottom of Hellas are ~240 K, relatively warmer than the rim at ~210 K (Figure 1c). Estimates of the current Hellas basin geothermal heat flux range from ~20 (Plesa et al. 2016) to >35 mW/m^2 (McGovern et al. 2004), with the likelihood that the flux has decreased by as much as a factor of two since the end of the Noachian (Montési & Zuber 2003, Solomon et al., 2005). Ruiz et al. (2011) estimate a minimum Noachian flux for the Hellas basin of ~55 mW/m^2 and we adopt that value for the modelled region.

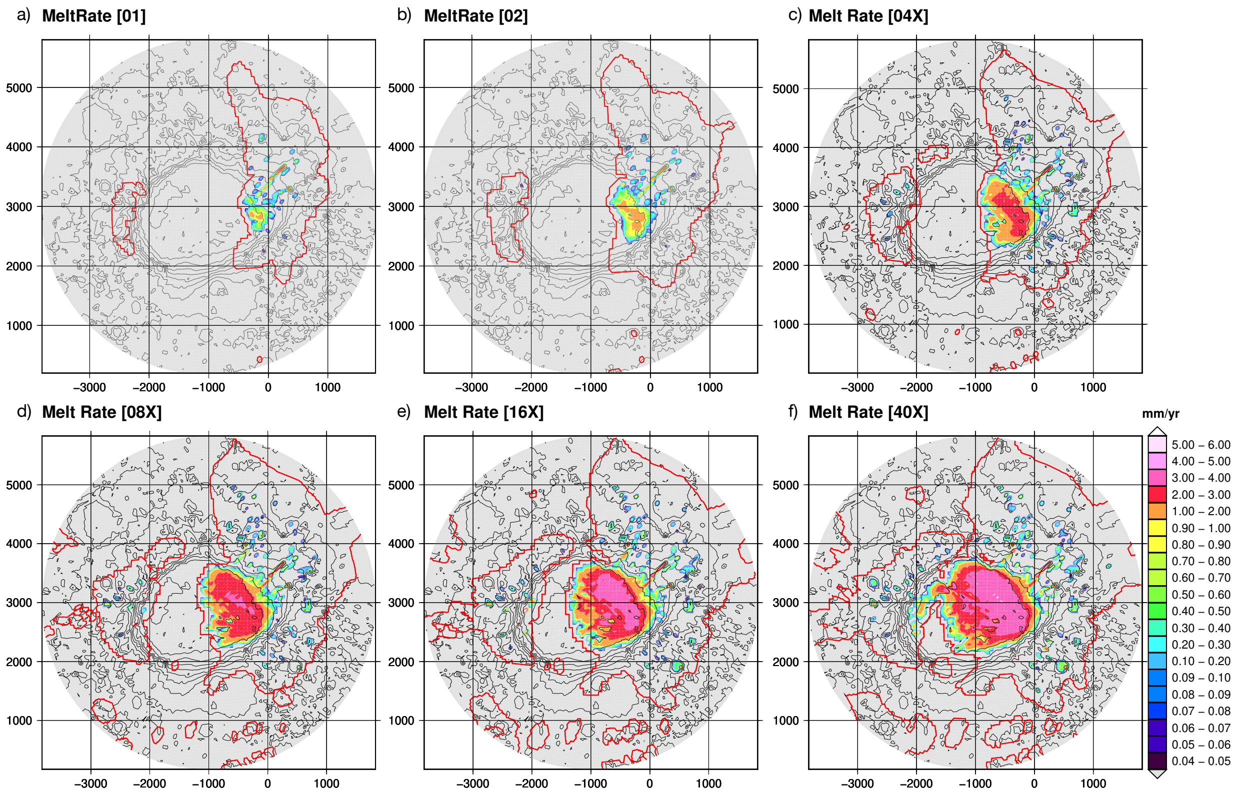

Figure 11: Basal melting rates where the bed reaches the pressure melting point for the various supply limits.

With shear heating contributing on the steeper basin wall slope, much of the bed reaches the melting point, liquid water is produced, and enhanced flow velocities due to sliding can occur (Figures 6b,e). Figure 10 shows the equilibrated ice thickness, Figure 11 the computed basal melting rate, and Figure 12 the resulting ice flow velocities for the sampled supply limits (1X to 40X). Of note are the numerous patches and corridors of relatively high-velocity ice flow features that follow inlet valleys on the basin wall. Since UMISM is using unmodified current topography we do acknowledge that these valleys were not in their present form at this time. However, glacial flow in this are may have been "pre-processed" by glacial flow-induced topography so that they became preferred pathways for later fluvial flow. With the relatively warmer basin floor surface temperatures (~240 K), much of the ice sheet bed is at the melting point. The thick ice at the base of the basin wall is also melted at the bed. The contribution due to shear heating is significant due to the relatively steeper surface slopes producing a high driving stress (Figure 7a). Of the four sampled supply limits, 16X and 40X are closest to the scarp edge of the ACP (16X slightly smaller; 40X slightly larger).

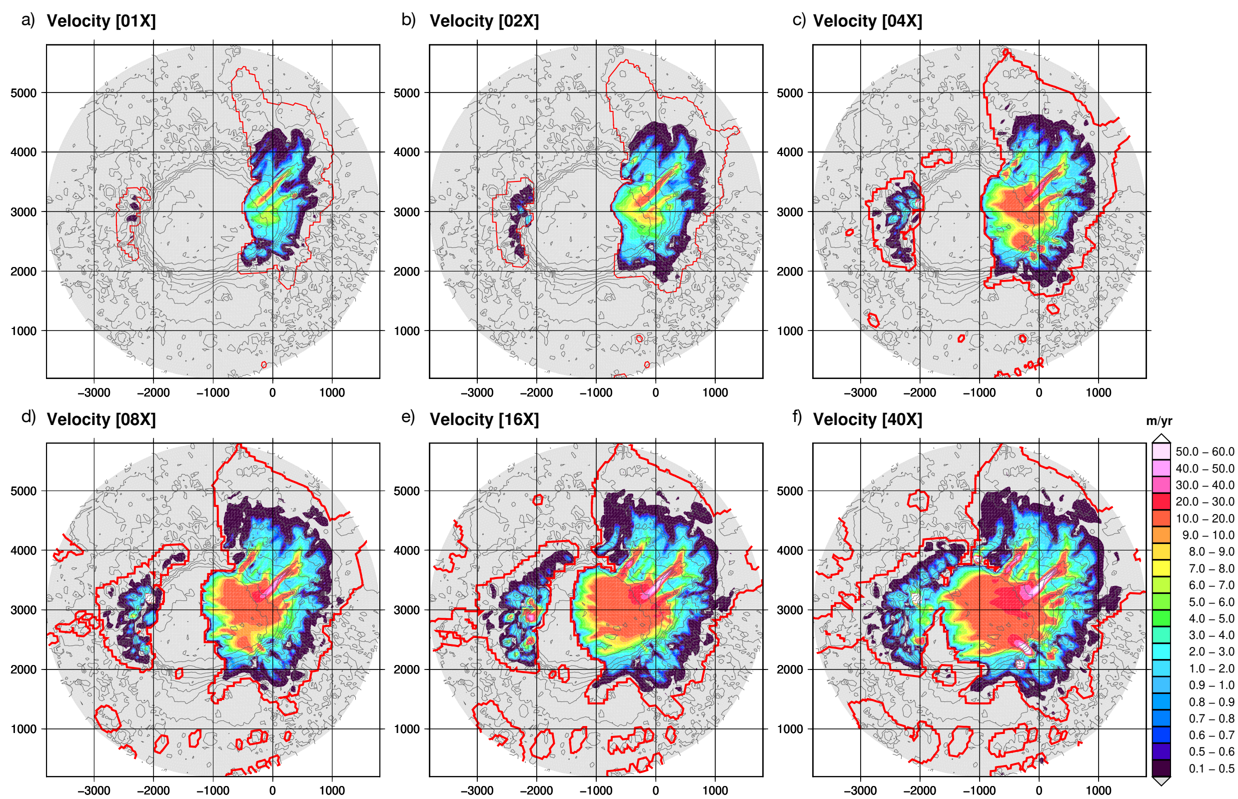

Figure 12: Ice velocity for the various supply limits.

4 Discussion

On the basis of our combined GCM results (1 bar atmospheric pressure, 42 degree obliquity, faint young sun) with the UMISM GFM analysis of the Hellas Glacial System, we synthesize the results and address the following series of questions in order to clarify the nature and distribution of the predicted glacial deposits and how we might assess these results in the future with further geological observations:

1. *What was the predicted areal distribution and thickness of ice accumulation on the eastern Hellas rim?*: The initial accumulation area footprint (Figure 1e) is 14 Mkm^2, 56% of the modelled region, and as the simulation starts, this area is immediately covered with accumulated ice so that for each supply limit the area of the initial ice sheet is close to this value. For each supply limited case, this ice cover initially decreases as the positive component of the net mass balance is decreased, as the volume increases toward the supply limit, resulting in movement toward the mass balance pattern shown in Figure 1f (the 16X supply limit at 1 Myr). In the 4X and 8X cases, this decrease is monotonic, with the areas of the 4X and 8X cases at 1 million years dropping to 7 and 9 MKm^2 respectively (Figure 3c).

Average thicknesses are similar for all supply cases, increasing monotonically, with most rapid thickening before 200,000 years, reaching 1400 m (4X) to 1529 m (5X) at 1 million years (Figure 6b). Total volumes also increase monotonically, again rapidly until 200,000 years, followed by slower growth until 1 million years, at which point volumes are 10 (4X) to 21 (40X) Mkm^3 (Figure 6c).

2. *How much of the ice sheet bed is predicted to melt?*: Initial average basal temperatures (Figure 1c), show little difference among the supply limit cases, all beginning at 214 K, and increasing to 247 K (4X) to 245 K (40X) (Figure 6d). The percent of the ice sheet bed area that reaches the melting point is 7.5% (4X) to 15% (40X) (Figure 6e). Melt rates (Figure 11) show average rates of 1.2 (4X) to 2.1 (40X) mm/year. Combining these with the simulation areas and percentages of bed melted, this yields a total basal meltwater production rate of 0.7 (4X) to 4.3 (40X) km^3/year that would potentially be released from beneath the ice sheet (Table 1; Figure 6).

3. *Under what conditions is significant ice flow predicted to begin and at what rates?*: Ice flow does not begin until the ice is sufficiently thick and has a surface slope to provide a driving stress (Figure 7a). Given that the GCM mass balance (Figure 1e) is maximum on the eastern Hellas wall, ice will thicken there first, with a slope determined by the mass balance spatial distribution and the underlying bed slope. Wall ice will flow preferentially downslope into the ablation area at the basin floor (Figures 1d,e,f). We find that the average velocity over the entire ice sheet increases linearly with the growing average thickness until average thickness reaches ~1000 m at ~400,000 years, after which it remains approximately constant for all four supply limit cases. Average velocity differs, reaching 1.8 m/year for the 4X case, to 3 m/year for the 40X case (Figure 6b). In areas where the bed is melted (Figure 11) velocities reach 10-20 m/yr with localized regions exceeding 40 m/yr (Figure 12). This compares to peak velocities in McMurdo Dry Valleys cold-based glaciers that approach ~40 mm/year (Rignot et al., 2002) showing the potential significance of wet-bed sliding in the Hellas basin region.

4. *How much is ice predicted to accelerate when it flows down the interior wall?*: The fastest flow occurs at maximum driving stress and produces shear-heating within the ice column, further softening the ice and further accelerating flow. With this additional warming, the bed reaches the melting point (while perchlorates can lower the melting point; Hecht et al., 2009; Sori and Bramson, 2019; the melting point is assumed to be 273 K), and lubricating meltwater is produced, leading to sliding (i.e. plug flow). This phenomenon is observed on the Hellas wall (Figure 11) in the form of patches, as well as linear "streaming" features (Figure 12), the largest of which corresponds to Dao Vallis. Internal temperatures increase with depth due to the basal geothermal flux and internal shear heating, so that where the ice is thick enough, the base of the bed can also reach the melting point. This condition is observed at the base of the basin wall, where ice reaches its maximum thickness (Figure 10), and this too produces lubricating melt water (Figure 11) leading to faster sliding (Figure 1d and Figure 12). Due to the basin floor being in the ablation zone, a companion effect is that warmer deep ice is brought to the surface by advection, warming and softening the overall ice column.

5. *What is the predicted location of non-ice debris and its provenance in the modeled Hellas Glacial System (HGS)?*: The locally mountainous topography of the Hellas basin rim (Hesperia Planum) displays numerous currently exposed peaks and massifs ranging up to 2-3.75 km above the plains surface (Ivanov et al., 2005; Head et al., 2005). Noachian ice thickness estimates are in the 1.4-1.5 km range, and so there should be numerous nunataks shedding debris down onto the ice surface to provide debris cover on adjacent HGS flowing ice. Additional debris cover

contributions come from impact crater ejecta (e.g., Schultz and Mustard, 2004), atmospheric dust (e.g., Kahre et al., 2017), and volcanic ash (e.g., Wilson and Head, 2009). Sublimating dusty ice has been shown to produce an armoring lag layer that can reach several meters thickness in under 1 million years (Figure 8 and 10; Schorghofer 2010). While such debris thicknesses are unknown for Mars, on the Mullins debris-covered glacier in the Antarctic Dry Valleys thicknesses reach ~50 cm (Marchant and Head, 2007). In addition, when the glacier accelerates and wet-based glaciation begins on the basin wall, underlying sediment and contributions from bedrock erosion are added to the base of the glacier. Thus, when the glacier reaches the basin floor it should be characterized by a surface debris cover and basal debris contributions from its wet-based phases.

6. *Is the Hellas floor component of the glacial landsystem predicted to cover the entire floor and what is its fate subsequent to the end of the active glacial phase?*: A large portion (~85%) of the Hellas basin floor is covered by the Alpheus Colles Plateau, which is bounded by a major scarp in the WNW portion of the current basin (Figure 1a). Berhardt et al. (2016a) identified two units within the ACP. The hummocky member Hih is thought to have resulted from a combination of fluvial, glacial, and aeolian processes sourced from Hesperia Planum, with the additional possibility of lava-ice interactions. The emplacement of the abundant lava flows that formed the subsequent Hesperian ridged plains may have resulted in large volumes of lava flowing out on top of the rim/wall/floor ice deposits, resulting in both contact melting, formed by the initial conductive transfer of heat from the lava flow to the ice substrate, and deferred melting, induced at a later time due to raising of the melting isotherm into the base of the ice deposit (e.g., Cassanelli & Head, 2016), as well as possible loading effects causing subsurface ice flow and surface deposit deformation (e.g., Fastook and Head, 2019). The knobby member Hik was possibly formed by loss of ground ice during retreat of an ice sheet. We hypothesize that the ACP scarp may represent the margin of a reworked and evolved remnant of the original debris-covered glacial floor deposit. Thickness maps (Figure 10) show that for the four sampled supply limits, basin floor cover is 31% (4X) to 88% (40X). While the GCM results define the floor of Hellas as an ablation area (Figure 1e,f), it is also relatively cold (Figure 1c) and ablation that occurs there may be dominated by sublimation rather than melting. In addition, as in the case of Amazonian glaciers (e.g., Head et al., 2005; Holt et al., 2008), the sublimation lag may significantly retard ablation and help preserve ice below the debris cover (Schorghofer 2010, Bramson et al, 2017).

7. *What is the predicted approximate thickness and volume of glacial ice thought to be on the Hellas floor at the end of active glacial growth?*: The modelled region (Figures 1, 10-12) has an area of 25.13 Mkm^2. Within that grid the ice cover ranges from 31% (4X) to 60% (40X). Average ice thickness is 1292 to 1417 m and total ice sheet volume is 10 to 21 Mkm^3 (71 to 147 m GEL) for the four cases.

Limiting our attention to only the Hellas basin floor (those points lower than -6200 m elevation), the basin floor area is 2.3 Mkm^2, and ice cover is 31 to 88% for the four cases. Average thickness on the basin floor is 1350 to 1761 m, with maximum thicknesses of 2591 to 3333 m for the four cases. Basin floor ice volumes range from 1 to 3.6 Mkm^3 (6.6 to 25 m GEL). This raises the possibility that significant amounts of ice may remain sequestered below glacial till on the basin floor, and unaccounted for in Noachian global water inventory estimates (e.g., Carr and Head, 2015).

8. *What are the factors producing basin floor meltwater and where, and how much meltwater is predicted to be produced?*: Much of the basin floor ice-covered area reaches the melting point at its base. Of the total basin floor area (2.3 Mkm^2), ~24% to 75% is melted, producing ~114 to 1473 km^3/yr of basal meltwater (~0.8 to 10 m GEL/Kyr). The basin floor is completely in the ablation area, and that can also potentially produce meltwater. Meltwater from top-down melting can follow several routes. 1) Melt water originating near the margin of the ice sheet can run off the surface onto the adjacent ice-free landscape, potentially ponding in topographic depressions. Given the low mean-annual temperatures these lakes would have frozen surfaces, and in some cases might be completely frozen. 2) If there is a significant firn layer in the upper reaches of the ice sheet, the meltwater can percolate into the firn. Given the low mean-annual temperatures this water can refreeze at depth, filling the firn pore space while at the same time delivering latent heat that warms the layer at which refreezing occurs. This added heat softens the ice allowing greater deformation and flow. As the pore space in the firn fills, making the ice less permeable, the meltwater will be more likely to flow off the surface of the ice onto the adjacent ice-free landscape. 3) Meltwater flowing across the surface of the ice sheet can form ponds, effectively insulating the ice sheet surface from diurnal temperature variation. Again, the low MAT means these ponds can refreeze, delivering latent heat to the upper layers of the ice sheet. 4) Ponds and surface streams can drain into moulins. As with percolation into firn, this meltwater can refreeze at depth, delivering latent heat, or it can reach the bed where it can refreeze or contribute to the basal meltwater hydrology, which can lead to enhanced flow and potential sliding on a lubricated bed. This additional meltwater volume ranges from ~138 to 325 km^3/yr (1 to 2.2 m GEL/Kyr).

9. *What is the predicted fate of top-down and bottom-up meltwater and could there have been a lake or sea associated with the emplacement of the Hellas Glacial Landsystem?*: Our GFM results predict that as much as 114 to 1473 km^3 per year of meltwater might be produced by basal melting for each of the four supply limits. This is in addition to the top-down melting from surface ablation dictated by the GCM results of Figure 1e,f (138-305 km^3 per year for the four cases). Basal meltwater could emerge laterally in front of the glacier on the NW Hellas floor, ascend to the surface locally due to overburden pressure, or freeze to the glacial base when the glacier transitioned to cold-based conditions. Surface meltwater can flow directly off the surface or contribute to basal lubrication, ultimately reaching the margin along with the basal meltwater. Despite being relatively warmer than the basin rim and wall, the basin floor MAT was well below 273K, suggesting that any meltwater at the surface was likely to be transient and would freeze relatively rapidly, then ablating and returning to snow out in the glacial accumulation areas.

10. *Does the interpreted current configuration of ice on the Hellas basin floor provide any information about the total active HGS duration and the Late Noachian global water budget?*: Simulations for all four supply limit cases were run for 1,000,000 years, at which point the HGS had reached a steady state. This is a balance where, as the ice sheet volume approaches the supply limit, the positive accumulation component of the mass balance is reduced. It is understood that debris cover can also reduce the negative ablation component (Bramson et al.

2017), however, our main concern is to account for the net mass balance as ice flows out of the accumulation area and into an ablation region. Our processing of the GCM results into separate accumulation and ablation components allows us to reduce accumulations as the supply limit is approached, but we leave the ablation unchanged as ablation is likely due to local conditions (latitude, elevation, season) and hence expresses the potential for mass removal at that specific location regardless of accumulation amount. It is true that the evolution of an ice sheet does have the potential to alter its own local climate, but this is beyond the scope of our simulation, as we are assuming a static climate from the GCM results for the simulation duration. A future improvement in our understanding would be to couple a circulation model with a glacial model so that as the ice sheet evolved, it would modify its own climate. Additionally, for simulations greater than 100,000 years, one would need to vary orbital parameters, in particular, obliquity, since that has a significant influence on the distribution of climate across Mars**.** As previously described, this results in a reduction of the positive mass balance area (Figures 1e,f). Steady state is achieved when any further area reduction results in a shrinking ice sheet, which then increases the accumulation component. Orbital parameters, in particular obliquity, vary on the order of 100,000 years, with an amplitude envelope of ~1.5 million years. The GCM we utilized employed an obliquity of 42 degrees, a value thought to be "most probable" for the Late Noachian-Early Hesperian (Laskar et al., 2004). On the basis of our analysis, the Hellas Glacial System would need at least a few 10^5 years to form and about 10^6 years to reach equilibrium. As is apparent from Figure 6c, each of the supply-limit cases (with the exception of 40X) achieve between 60 and 80% of their equilibrium volumes within the first 10^5 years and 85 to 90% within 2 x 10^5 years. The HGS is related to the atmospheric pressure-induced adiabatic cooling effect typical of early Mars (Wordsworth et al., 2013), modulated by obliquity variations (Laskar et al, 2004), and thus the duration of the HGS could have been in the 10^6-10^8 year range, a duration not uncommon in Earth's glacial history (Crowell, 1999).

Noachian glacial ice may remain sequestered on the Hellas basin floor below a protective sublimation till cover, and unaccounted for in current water budget estimates (e.g., Carr and Head, 2015). In the 4X case, which corresponds to 136 m GEL, over half is contained in the equilibrium Hellas Glacial Landsystem. Of that, 6.6 m GEL (close to 5%) are on the basin floor where some fraction is potentially covered by debris and effectively removed from the active atmosphere. Hellas floor volume predictions for other supply limits are 8X (11 m GEL), 16X (17 m GEL), and 40X (25 m GEL). Thus, any ice deposits currently sequestered below the surface of the Hellas basin floor should be added to the Late Noachian-Early Hesperian global water budget estimates of Carr and Head (2015).

Also uncertain is the cause and timing of the demise of the Hellas Glacial System, and the role played by the immediately following Early Hesperian phase of global volcanism (e.g., Carr and Head, 2010). More detailed stratigraphic analysis of the relationship between Hesperian ridged volcanic plains and related deposits, and the substrate on which they were emplaced, using criteria outlined in Cassinelli and Head (2016), could help determine if there was a Late Noachian-Early Hesperian Hellas Glacial System, and if so, whether these volcanic events might have led to its demise. For example, the lava flows that formed the Hesperian ridged plains may have resulted in large volumes of lava flowing out on top of the ice deposits, producing significant contact and deferred melting (e.g., Cassanelli & Head, 2016), and possible loading effects causing subsurface ice flow and surface deposit deformation (e.g., Fastook and Head, 2019). Furthermore, Hesperian lava flows superposed on the eastern Hellas rim glaciers could have produced significant volumes of meltwater (e.g., Cassanelli and Head, 2016; 2018), forming associated outflow channels and contributing to the demise of the HGS. These prediction serve as further assessments of the prediction of the model outlined here.

5 Conclusions

On the basis of our analysis of the accumulation and flow of ice on the rim of the Hellas basin utilizing predictions from Late Noachian GCM, we conclude that significant ice accumulation could have occurred on the eastern basin rim and that the relatively steep basin wall slopes would produce significant glacial flow down onto the basin floor. Basin wall slopes are sufficiently steep that shear heating would cause areas of the glacier bed to reach the melting point and wet-based glacial conditions to ensue, further enhancing flow velocities. Such wet-based conditions along the walls could have caused significant substrate erosion. If the cold and icy climate predicted by the GCMs was the ambient climate for any significant part of the ~400 Ma-long Noachian, such substrate erosion may be partly responsible for the missing mass (Tanaka et al., 2002; Ivanov et al., 2005) and unusual shape of the Hellas basin rim and wall in this direction (Figure 1a), and deposition of significant volumes of material removed from the basin wall onto the basin floor.

In addition, thicker ice and rising geotherms on the eastern basin floor would produce wet-based glaciers that would have proceeded to flow out onto the basin floor and cover a significant part of the floor (Figures 10, 11), the extent depending on supply limitations. Basal and surface meltwater are predicted to have readily drained onto the basin floor beyond the ice margin and may have formed a large lake/sea, with the total volume of meltwater being supply and temperature-limited. Despite the relatively higher atmospheric surface temperatures on the deep floor of Hellas (Palumbo and Head, 2019), a Hellas floor lake/sea surface would have been ice covered for most of the year. Under these conditions, the hydrological system is predicted to be horizontally stratified (shear heating itself on the walls does not melt the cryosphere), except possibly on the eastern basin floor (the locations of thickest ice/basal melting; Figures 1d, 10-12) where ice might be thick enough to remove the interstitial ice in the bedrock below the HGS if it remained for a sufficient duration (Palumbo & Head 2019).

Our analysis highlights a number of outstanding questions that can help assess both the ‘cold and icy’ early Mars climate model, and the Hellas Glacial System model presented here, and further investigate their possible implications. Could the HGS have been responsible for the glacial erosion of sufficient debris to account for the missing mass on Hesperia Planum (e.g., Ivanov et al., 2005; Tanaka et al., 2002)? Could the routes of the later fluvial channels on the eastern Hellas wall have been “pre-processed” by focused glacial basal erosion? Is the hypothesized amount of meltwater produced similar to the volumes and timing for interpreted ancient seas (e.g., Moore and Wilhelms, 2001) or are additional sources needed? Is there any evidence for the presence of residual buried glacial ice revealed in the topography, geomorphology and stratigraphy of the currently observed geological units on the floor of Hellas (e.g. Bernhardt et al., 2016a,b). What is the origin of the low topography on the NW Hellas basin floor, and could the “honeycomb and banded terrain” seen there (e.g., Weiss and Head, 2017; Bernhardt et al., 2019) represent deformation of ancient residual glacial ice?

The sequence of events outlined in our HGS model and associated geomorphic processes provide a series of predictions that can be specifically assessed with detailed analyses of observational data for geomorphic features and stratigraphy of the Hellas basin. For example, buried glacial and frozen lake ice may be the layer seen deforming to produce diapiric-like structures on the basin floor (Bernhardt et al. 2016a, 2016b, 2019; Diot et al., 2016; Weiss & Head 2017); this "honeycomb terrain" in the deepest area of the western basin floor (the dark purple -7.5 to -7 km elevation; Figure 1a) is believed to have formed prior to the emplacement of the Hesperian-ridged plains, between ~3.7 Ga and 4 Ga (Bernhardt et al. 2016a, 2016b), and may offer a constraint on the timing of circum-Hellas glaciation. Unfortunately, the vast majority of Hellas floor SHARAD detections are due to roughness-induced clutter (e.g., Cook at al., 2020); any remaining HGS ice is likely buried beneath several meters of sublimation till, superposed volcanic plains and other units, making radar detection difficult. Furthermore, the western, northern and southern Hellas walls and rim have been the subject of many geological analyses (e.g., Tanaka and Leonard, 1995; Tanaka et al., 2014) and if the Hellas Glacial System was indeed present, as modeled in this analysis, the possible presence of the HGS in these areas, and assessment with the consistency of these geologic and stratigraphic studies, should be undertaken (e.g., see summary in Boatwright and Head, 2023).

Acknowledgments: We gratefully acknowledge the discussions, advice and assistance of K. Scanlon, A. Palumbo, J. Cassanelli, D. Weiss, F. Forget and R. Wordsworth. Detailed assessments and suggestions by two reviewers and the Editor significantly improved and clarified aspects of this contribution. We would particularly like to thank Dr. Victor Baker for his extensive and detailed review, which helped to improve the clarity and relevance of our presentation, discussion and conclusions.

Data Availability Statement

Topography for UMISM was obtained from MOLA data (Smith et al. 2001) available here: https://astrogeology.usgs.gov/search/details/Mars/GlobalSurveyor/MOLA/Mars_MGS_MOLA_DEM_mosaic_global_463m/cub.

Smith, D. E., Zuber, M. T., Frey, H. V., Garvin, J. B., Head, J. W., Muhleman, D. O., Pettengill, G. H., et al. (2001). Mars Orbiter Laser Altimeter—Experiment summary after the first year of global mapping of Mars. *Journal of Geophysical Research, 106*(E10), 23689–23722. https://doi.org/10.1029/2000JE001364

Figures were developed using Generic Mapping Tools (https://www.generic-mapping-tools.org) and Gnuplot (http://www.gnuplot.info).

Mars Subsurface Ice Model (MSIM) Program Collection, version 1.2.0, available from github here https://github.com/nschorgh/MSIM/

The University of Maine Ice Sheet Model (UMISM, Fastook & Prentice 1994) adapted for Mars is archived on *Zenodo* (Fastook 2023a).

Fastook, J. L., and M. Prentice (1994), A finite-element model of Antarctica: Sensitivity test for meteorological mass balance relationship, *Journal of Glaciology*, 40 (134), 167–175.

Fastook, James. (2023a). UMISM software. *Zenodo*. https://doi.org/10.5281/zenodo.8031076.

Results from UMISM generated for this paper are archived on *Zenodo* (Fastook 2023b).

Fastook, James. (2023b). Hellas Results [Data set]. *Zenodo*. https://doi.org/10.5281/zenodo.8031135.

References

Becker, E., G. Carey, and J. Oden (1981), *Finite Elements, An Introduction*, Prentice-Hall, Englewood Cliffs.

Benn, D., and D. J. Evans (2014), *Glaciers and Glaciation*, Routledge.

Bernhardt, H., H. Hiesinger, M. Ivanov, O. Ruesch, G. Erkeling, and D. Reiss (2016a), Photogeologic mapping and the geologic history of the Hellas Basin floor, Mars, *Icarus*, 264, 407–442, http://dx.doi.org/10.1016/j.icarus.2015.09.031.

Bernhardt, H., D. Reiss, H. Hiesinger, and M. A. Ivanov (2016b), The honeycomb terrain on the Hellas basin floor, Mars: A case for salt or ice diapirism, *Journal of Geophysical Research: Planets*, 121, 714–738, doi:10.1002/ 2016JE005007.

Bernhardt, H., D. Reiss, M. Ivanov, E. Hauber, H. Hiesinger, J. Clark, and R. Orosei (2019), The banded terrain on northwestern Hellas Planitia: New observations and insights into its possible formation, *Icarus*, 321, 171–188, https://doi.org/10.1016/j.icarus.2018.11.007.

Boatwright, B. D., and J. Head (2023), Hellas Basin witness plate: Sequence and timing of altitude-dependent glacial features on early Mars, *Lunar and Planetary Science Conference 54*, #1248.

Bramson, A. M., S. Byrne, and J. Bapst (2017), Preservation of midlatitude ice sheets on Mars, *Journal of Geophysical Research Planets*, 122, 2250–2266, https://doi.org/10.1002/2017JE005,357.

Brough, S., B. Hubbard, C. Souness, P. M. Grindrod, and J. Davis (2016), Landscapes of polyphase glaciation: eastern Hellas Planitia, *Journal of Maps*, 12(3), 530–542, http://dx.doi.org/10.1080/17445,647.2015.1047,907.

Cardenas, B. T., and M. P. Lamb (2022), Paleogeographic reconstructions of an ocean margin on Mars based on deltaic sedimentology at Aeolis Dorsa, *Journal of Geophysical Research Planets*, 127(10), e2022JE007,390, https://doi–org.wv–o–ursus–proxy02.ursus.maine.edu/10.1029/2022JE007,390.

Carr, M., and J. Head (2010), Geologic history of Mars, *Earth and Planetary Science Letters*, 294(3-4), 185–203, doi:10.1016/j.epsl.2009.06.042.

Carr, M. H., and J. W. Head (2014), Martian unbound water inventories: Changes with time, *Lunar and Planetary Science Conference XLV*, (#1427).

Carr, M. H., and J. W. Head (2015), Martian surface/near-surface water inventory: Sources, sinks, and changes with time, *Geophysical Research Letters*, 42, 726–732, doi:10.1002/2014GL062464.

Cassanelli, J. P., and J. W. Head (2016), Lava heating and loading of ice sheets on early Mars: Predictions for meltwater generation, groundwater recharge, and resulting landforms, *Icarus*, 271, 237–264, http://dx.doi.org/10.1016/j.icarus.2016.02.004.

Cassanelli, J. P., and J. W. Head (2018), Formation of outflow channels on Mars: Testing the origin of Reull Vallis in Hesperia Planum by large-scale lava-ice interactions and top-down melting, *Icarus*, 305, 56–79, doi: 10.1016/j.icarus.2018.01.001.

Cleland, C. (2001). Historical science, experimental science, and the scientific method. *Geology*, 29(11), 987-990, https://doi.org/10.1130/0091–7613(2001)029<0987:HSESAT>2.0.CO;2.

Cleland, C. (2002), Methodological and epistemic differences between historical and experimental science, *Philosophy of Science*, 69, 474–496, https://doi.org/10.1086/342,455.

Cook, C. W., A. M. Bramson, S. Byrne, J. W. Holt, M. S. Christoffersen, D. Viola, C. M. Dundas, and T. A. Goudge (2020), Sparse subsurface radar reflectors in Hellas Planitia, Mars, *Icarus*, 348, 113,847, https://doi.org/10.1016/j.icarus.2020.113847.

Craddock, R. A., and A. D. Howard (2002), The case for rainfall on a warm, wet early Mars, *Journal of Geophysical Research*, 107(E11), 21–36, doi:10.1029/2001JE001,505.

Crowell, J. C. (1999), Pre-Mesozoic ice ages, their bearing on understanding the climate system, *Memoir Geological Society of America*, 192, 1–122.

Crown, D., K. H. Price, and R. Greeley (1992), Geologic evolution of the east rim of the Hellas basin Mars, *Icarus*, 100(1), 1–25, https://doi.org/10.1016/0019– 1035(92)90,014–X.

Crown, D. A., L. F. Bleamaster III, and S. C. Mest (2005), Styles and timing of volatile-driven activeity in the eastern Hellas region of Mars, *Journal of Geophysical Research Planets*, 110, E12S22, doi:10.1029/2005JE002,496.

Diot, X., M. R. El-Maarry, F. Schlunegger, K. P. Norton, N. Thomas, P. M. Grindrod, , and M. Chojnacki (2016), Complex geomorphologic assemblage of terrains in association with the banded terrain in Hellas basin, Mars, *Planetary and Space Science*, 121, 36–52, https://doi.org/10.1016/j.pss.2015.12.003.

Fassett, C. I., and J. W. Head (2011), Sequence and timing of conditions on early Mars, *Icarus*, 211, 1204–1214, https://doi.org/10.1016/j.icarus.2010.11.014.

Fastook, J. L., and J. W. Head (2013), Amazonian non-polar glaciation: Supply-limited glacial history and the role of ice sequestration, *Lunar and Planetary Science Conference XLIV*, (#1256).

Fastook, J. L., and J. W. Head (2014), Amazonian mid- to high-latitude glaciation on Mars: Supply-limited ice sources, ice accumulation patterns, and concentric crater fill glacial flow and ice sequestration, *Planetary and Space Science*, 91, 60–76 http://dx.doi.org/10.1016/j.pss.2013.12.002.

Fastook, J. L., and J. W. Head (2015), Glaciation in the Late Noachian Icy Highlands: Ice accumulation, distribution, flow rates, basal melting and top-down melting rates and patterns, *Planetary and Space Science*, 106, 82–98, http://dx.doi.org/10.1016/j.pss.2014.11.028.

Fastook, J. L., and J. W. Head (2019), Lava loads superposed on martian glaciers: An assessment of ice-flow velocity enhancements, *Lunar and Planetary Science Conference 50*, #1345.

Fastook, J. L., J. W. Head, D. R. Marchant, and F. Forget (2008), Tropical mountain glaciers on Mars: Altitude-dependence of ice accumulation, accumulation conditions, formation times, glacier dynamics, and implications for planetary spin-axis/orbital history, *Icarus*, 198, 305–317, doi.org/10.1016/j.icarus.2008.08.008.

Fastook, J. L., J. W. Head, F. Forget, J.-B. Madeleine, and D. R. Marchant (2011), Evidence for Amazonian northern mid-latitude regional glacial landsystems on Mars: Glacial flow models using GCM-driven climate results and comparisons to geological observations, *Icarus*, 216, 23–39, doi.org/10.1016/j.icarus.2011.07.018.

Fastook, J. L., J. W. Head, D. R. Marchant, F. Forget, and J.-B. Madeleine (2012), Early Mars climate near the Noachian-Hesperian boundary: Independent evidence for cold conditions from basal melting of the South Polar Ice Sheet (Dorsa Argentea Formation) and implications for valley network formation, *Icarus*, 219, 25–40, https://doi.org/10.1016/j.icarus.2012.02.013.

Fastook, J. L., J. W. Head, and D. R. Marchant (2014), Formation of Lobate Debris Aprons on Mars: Assessment of regional ice sheet collapse and debris-cover armoring, *Icarus*, 228, 54–63, doi: http://dx.doi.org/ 10.1016/j.icarus.2013.09.025.

Fastook, J. L., and M. Prentice (1994), A finite-element model of Antarctica: Sensitivity test for meteorological mass balance relationship, *Journal of Glaciology*, 40 (134), 167–175, https://doi.org/10.3189/S0022143000003944.

Forget, F., R. M. Haberle, F. Montmessin, B. Levrard, and J. W. Head (2006), Formation of glaciers on Mars by atmospheric precipitation at high obliquity, *Science.*, 311(5759), 368–371, doi:10.1126/science.1120,335, doi:doi:10.1126/science.1120335.

Forget, F., R. Wordsworth, E. Millour, J.-B. Madeleine, L. Kerber, J. Leconte, E. Marcq, and R. Haberle (2013), 3D modelling of the early martian climate under a denser CO2 atmosphere: Temperatures and CO2 ice clouds, *Icarus*, 222, 81–99, http://dx.doi.org/10.1016/j.icarus.2012.10.019.

Grott, M., and D. Breuer (2010), On the spatial variability of the Martian elastic lithosphere thickness: Evidence for mantle plumes?, *Journal of Geophysical Research*, 115, , E03,005, doi:10.1029/2009JE003,456, 2010.

Haberle, R. M., C. P. McKay, J. Schaeffer, N. A. Cabrol, E. A. Grin, A. P. Zent, and R. Quinn (2001), On the possibility of liquid water on present-day Mars, *Journal of Geophysical Research Planets*, 106(E10), 23,317–23,326, https://doi.org/10.1029/2000JE001,360.

Head, J. W. (2012), Mars climate history: A geological perspective, in *43rd Annual Lunar and Planetary Science Conference*, 1659, p. 2137.

Head, J. W., G. Neukum, R. Jaumann, H. Hiesinger, E. Hauber, M. Carr, P. Masson, B. Foing, H. Hoffmann, M. Kreslavsky, S.Werner, S. Milkovich, S. van Gasselt, and T. H. C.-I. Team (2005), Head et al. reply to "are there active glaciers on Mars?", *Nature*, 438, E10, https://doi.org/10.1038/nature04358.

Hecht, M. H., S. P. Kounaves, R. C. Quinn, S. J. West, S. M. M. Young, D. W. Ming, D. C. Catling, B. C. Clark, W. V. Boynton, J. Hoffman, L. P. DeFlores, Gospodinova, J. Kapit, and P. H. Smith (2009), Detection of perchlorate and the soluble chemistry of martian soil at the Phoenix Lander site, *Science*, 325, 64–67, https://www.science.org/doi/10.1126/science.1172,466.

Holt, J. W., A. Safaeinili, J. J. Plaut, J. W. Head, R. J. Phillips, R. Seu, S. D. Kempf, P. Choudhary, D. A. Young, N. E. Putzig, D. Biccari, and Y. Gim (2008), Radar sounding evidence for buried glaciers in the southern mid-latitudes of Mars, *Science*, 322(5905), 1235–1238, doi:10.1126/science.1164246.

Ivanov, M. A., J. Korteniemi, V.-P. Kostama, M. Aittola, J. Raitala, M. Glamoclija, L. Marinangeli, and G. Neukum (2005), Major episodes of the hydrologic history in the region of Hesperia Planum, Mars, *Journal of Geophysical Research Planets*, 110, E12S21, doi:10.1029/2005JE002420.

Ji, L., T. Liu, V. R. Baker, and W. Luo (2023), Machine learning analyis of Martian valley networks: Paleoclimatic implications, P51D-2723, American Geophysical Union meeting, December, 2023 (Abstract).

Kadish, S. J., J. W. Head, and N. G. Barlow (2010), Pedestal crater heights on Mars: A proxy for the thicknesses of past, ice-rich, Amazonian deposits, *Icarus*, 210 (1), 92–101, doi.org/10.1016/j.icarus.2010.06.021.

Kahre, M. A., R. M. Haberle, J. L. Hollingsworth, , and M. J. Wolff (2020), MARCI-observed clouds in the Hellas Basin during northern hemisphere summer on Mars: Interpretation with the NASA/Ames Legacy Mars Global Climate Model, Icarus, 338, 113,512, https://doi.org/10.1016/j.icarus.2019.113,512.

Kahre, M. A., J. R. Murphy, C. E. Newman, R. J. Wilson, B. A. Cantor, M. T. Lemmon, and M. J. Wolff (2017), The Mars dust cycle, in *The Atmosphere and Climate* *of Mars,* vol. 18, edited by R. M. Haberle, R. T. Clancy, F. Forget, M. D. Smith, and R. W. Zurek, pp. 295–337, https://doi.org/10.1017/9781139060,172, Cambridge University Press.

Kamada, A., T. Kuroda, T. Kodama, Y. Kasaba, and N. Terada (2022), Evolution of ice sheets on early Mars with subglacial river systems, *Icarus*, pp. 115,117, https://doi.org/10.1016/j.icarus.2022.115117.

Kargel, J. S., and R. G. Strom (1992), Ancient glaciation on Mars, *Geology*, 20, 3–7.

Laskar, J., A. Correia, M. Gastineau, F. Joutel, B. Levrard, and P. Robutel (2004), Long term evolution and chaotic diffusion of the insolation quantities of Mars, *Icarus*, 170 (2), 343–364, doi.org/10.1016/j.icarus.2004.04.005.

Leonard, G. J., and K. Tanaka (2001), Geologic map of the Hellas region of Mars, *U.S. Geological Survey Geologic Investigations Series I–2694*, Pamphlet 10, US Department of the Interior, US Geological Survey, https://pubs.usgs.gov/imap/i2694/.

Luo, W., X. Cang, and A. D. Howard (2017), New martian valley network volume estimate consistent with ancient ocean and warm and wet climate, *Nature Communications*, 8(1), 15,766.

Marchant, D. R., and J. W. Head (2007), Antarctic dry valleys: Microclimate zonation, variable geomorphic processes, and implications for assessing climate change on Mars, *Icarus*, 192(1), 187–222, doi:10.1016/j.icarus.2007.06.018.

McGovern, P. J., S. C. Solomon, D. E. Smith, M. T. Zuber, M. Simons, M. A. Wieczorek, R. J. Phillips, G. A. Neumann, O. Aharonson, and J. W. Head (2004), Correction to "Localized gravity/topography admittance and correlation spectra on Mars: Implications for regional and global evolution", *Journal of Geophysical Research*, 109(E7), E07,007, doi:10.1029/2004JE002286.

Mest, S. C., and D. A. Crown (2001), Geology of the Reull Vallis region, Mars, *Icarus*, 153(1), 89–110, https://doi.org/10.1006/icar.2001.6655.

Millour, E., F. Forget, A. Spiga, M. Vals, V. Zakharov, L. Montabone, F. Lefèvre, F. Montmessin, J.-Y. Chaufray, M. A. López-Valverde, F. González-Galindo, S. R. Lewis, P. L. Read, M.-C. Desjean, F. Cipriani, and the MCD development team (2018), The Mars Climate Database (version 5.3), *MARS Science Workshop 'From Mars Express to Exomars'*, ESA-ESAC, Madrid, Spain.

Montési, L. G., and M. T. Zuber (2003), Clues to the lithospheric structure of Mars from wrinkle ridge sets and localization instability, *Journal of Geophysical Research*, 108(E6), 5048, doi:10.1029/2002JE001974.

Moore, J. M., and D. E. Wilhelms (2001), Hellas as a possible site of ancient ice-covered lakes on Mars, *Icarus*, 154, 258–276, doi:10.1006/icar.2001.6736.

Palumbo, A. M., and J. W. Head (2019), Oceans on Mars: The possibility of a Noachian groundwater-fed ocean in a sub-freezing martian climate, *Icarus*, 331, 209–225, https://doi.org/10.1016/j.icarus.2019.04.022.

Palumbo, A. M., J. W. Head, and R. D. Wordsworth (2018), Late Noachian Icy Highlands climate model: Exploring the possibility of transient melting and fluvial/lacustrine activity through peak annual and seasonal temperatures, *Icarus*, 300, 261–286, https://doi.org/10.1016/j.icarus.2017.09.007.

Plesa, A.-C., M. Grott, N. Tosi, D. Breuer, T. Spohn, and M. A. Wieczorek (2016), How large are present-day heat flux variations across the surface of Mars?, *Journal of Geophysical Research Planets*, 121, 2386–2403, doi:10.1002/2016JE005126.

Ramirez, R. M., and R. A. Craddock (2018), The geological and climatological case for a warmer and wetter early Mars, *Nature Geoscience*, 11, 230–237, https://doi.org/10.1038/s41,561–018–0093–9.

Ramirez, R. M., R. Kopparapu, M. E. Zugger, T. D. Robinson, R. Freedman, and J. F. Kasting (2014), Warming early Mars with CO_2 and H_2, *Nature Geoscience*, 7, 59–63, https://doi.org/10.1038/ngeo2000.

Ramirez, R. M., R. A. Craddock, and T. Usui (2020), Climate simulations of early Mars with estimated precipitation, runoff, and erosion rates, *Journal of Geophysical Research: Planets*, 125 (3), e2019JE006,160, https://doi.org/10.1029/2019JE006,160.

Rignot, E., B. Hallet, and A.Fountain (2002), Rock glacier surface motion in Beacon Valley, Antarctica, from synthetic-aperature radar interferometry, *Geophysical Research Letters*, 29 (12), 1–4, doi:10.1029/2001GL013494.

Rosenberg, E. N., A. M. Palumbo, J. P. Cassanelli, J. W. Head, and D. K. Weiss (2019), The volume of water required to carve the martian valley networks: Improved constraints using updated methods, *Icarus*, 317, 379–387, https://doi.org/10.1016/j.icarus.2018.07.017.

Ruiz, J., P. J. McGovern, A. Jiménez-Díaz, V. López, J.-P. Williams, B. C. Hahn, and R. Tejero (2011), The thermal evolution of Mars as constrained by paleo-heat flows, *Icarus*, 215(2), 508–517, doi:10.1016/j.icarus.2011.07.029.

Scanlon, K. E. (2016), *Ice sheet melting throughout mars climate history: Mechanisms, rates, and implications*, Ph.D. thesis, Brown University, Providence, RI.

Scanlon, K. E., J. W. Head, J. L. Fastook, and R. D. Wordsworth (2018), The Dorsa Argentea Formation and the Noachian-Hesperian climate transition, *Icarus*, 299, 339–363, http://dx.doi.org/10.1016/j.icarus.2017.07.031.

Schorghofer, N. (2007), Dynamics of ice ages on mars, *Nature*, 449, 192–195, doi:10.1038/nature06,082.

Schorghofer, N. (2010), Fast numerical method for growth and retreat of subsurface ice on Mars, *Icarus*, 208, 598–507, doi:10.1016/j.icarus.2010.03.022.

Schultz, P. H., and J. F. Mustard (2004), Impact melt and glasses on Mars, *Journal of Geophysical Research Planets*, 109, E01,001, doi:10.1029/2002JE002.

Solomon, S. C., O. Aharonson, J. M. Aurnou, W. B. Banerdt, M. H. Carr, A. J. Dombard, H. V. Frey, M. P. Golombek, S. A. Hauck, J. W. Head, B. M. Jakosky, C. L. Johnson, P. J. McGovern, G. A. Neumann, R. J. Phillips, D. E. Smith, and M. T. Zuber (2005), New perspectives on ancient Mars, *Science*, 307, 1214–1220, DOI: 10.1126/science.1101812.

Sori, M. M., and M. Bramson (2019), Water on Mars, with a grain of salt: Local heat anomalies are required for basal melting of ice at the South Pole today, Geophysical Research Letters, 46(3), 1222–1231, https://doi-org.wv-o-ursus-proxy02.ursus.maine.edu/10.1029/2018GL080,985.

Steakley, K. E., M. A. Kahre, R. M. Haberle, and K. J. Zahnle (2023), Impact induced H_2-rich climates on early Mars explored with a global climate model, *Icarus*, 394, 115,401, https://doi.org/10.1016/j.icarus.2022.115,401.

Tanaka, K. L., and G. L. Leonard (1995), Geology and landscape evolution of the Hellas region of Mars, *Journal of Geophysical Research*, 100(5407-5432), https://doi.org/10.1029/94JE02804.

Tanaka, K. L., J. S. Kargel, D. J. MacKinnon, T. M. Hare, and N. Hoffman (2002), Catastrophic erosion of Hellas Basin rim on Mars induced by magmatic intrusion into volatile-rich rocks, *Geophysical Research Letters*, 29(8), 1–37, https://doi.org/10.1029/2001GL013885.
.

Tanaka, K. L., J. A. Skinner, J. M. Dohm, R. P. Irwin III, E. J. Kolb, C. M. Fortezzo, T. Platz, G. G. Michael, and T. M. Hare (2014), *Geologic Map of Mars*, Report, U.S. Geological Survey, Reston, VA.

Voelker, M., E. Hauber, K. Stephan, , and R. Jaumann (2018), Volcanic flows versus water- and ice-related outburst deposits in eastern Hellas: A comparison, *Icarus*, 307, 1–16, https://doi.org/10.1016/j.icarus.2018.02.023.

Weiss, D. K., and J. W. Head (2017), Salt or ice diapirism origin for the honeycomb terrain in Hellas basin, Mars?: Implications for the early martian climate, *Icarus*, 284, 249–263, doi:10.1016/j.icarus.2016.11.016.

Wichman, R. W., and P. H. Schultz (1989), Sequence and mechanisms of deformation around the Hellas and Isidis Impact Basins on Mars, *Journal of Geophysical Research Solid Earth*, 94(B12), 17,333–17,357, https://doi.org/10.1029/JB094iB12p17333.

Williams, D. A., R. Greeley, R. L. Fergason, R. Kuzmin, T. B. McCord, J.-P. Combe, J. W. Head, L. Xiao, L. Manfredi, F. Poulet, P. Pinet, D. Baratoux, J. J. Plaut, J. Raitala, G. Neukum, and the HRSC Co-Investigator Team (2009), The circum-Hellas volcanic province, Mars: Overview, *Planetary and Space Science*, 57, 895–916, doi:10.1016/j.pss.2008.08.010.

Wilson, L., and J. W. Head (2009), Tephra deposition on glaciers and ice sheets on Mars: Influence on ice survival, debris content and flow behavior, *Journal of Volcanology and Geothermal Research*, 185, 290–297, doi:10.1016/j.jvolgeores.2008.10.003.

Wordsworth, R., F. Forget, E. Millour, J. Head, J.-B. Madeleine, and B. Charnay (2013), Global modelling of the early martian climate under a denser CO2 atmosphere: Water cycle and ice evolution, *Icarus*, 222, 1-19, http://dx.doi.org/10.1016/j.icarus.2012.09.036.